



A MODEL HIERARCHY FOR PREDICTING THE FLOW IN STIRRED TANKS WITH PHYSICS-INFORMED NEURAL NETWORKS

VERONIKA TRÁVNÍKOVÁ^{✉*1}, DANIEL WOLFF^{✉*1,2}, NICO DIRKES^{✉1},
STEFANIE ELGETI^{✉3}, ERIC VON LIERES^{✉4,5}, AND MAREK BEHR^{✉1}

¹Chair for Computational Analysis of Technical Systems, RWTH Aachen University, Germany

²Institute for Mathematics and Computer-Based Simulation, University of the Bundeswehr Munich, Germany

³Institute for Lightweight Design and Structural Biomechanics, TU Wien, Austria

⁴Institute of Bio- and Geosciences 1: Biotechnology, Forschungszentrum Jülich, Germany

⁵Computational Systems Biotechnology, RWTH Aachen University, 52074 Aachen, Germany

(Communicated by Handling Editor)

ABSTRACT. This paper explores the potential of **Physics-Informed Neural Networks (PINNs)** to serve as **Reduced Order Models (ROMs)** for simulating the flow field within **stirred tank reactors (STRs)**. We solve the two-dimensional stationary Navier-Stokes equations within a geometrically intricate domain and explore methodologies that allow us to integrate additional physical insights into the model. These approaches include imposing the Dirichlet **boundary conditions (BCs)** strongly and employing **domain decomposition (DD)**, with both overlapping and non-overlapping subdomains. We adapt the **Extended Physics-Informed Neural Network (XPINN)** approach to solve different sets of equations in distinct subdomains based on the diverse flow characteristics present in each region. Our exploration results in a hierarchy of models spanning various levels of complexity, where the best models exhibit ℓ_1 prediction errors of less than 1% for both pressure and velocity. To illustrate the reproducibility of our approach, we track the errors over repeated independent training runs of the best identified model and show its reliability. Subsequently, by incorporating the stirring rate as a parametric input, we develop a fast-to-evaluate model of the flow capable of interpolating across a wide range of Reynolds numbers. Although we exclusively restrict ourselves to **STRs** in this work, we conclude that the steps taken to obtain the presented model hierarchy can be transferred to other applications.

1. Introduction. **Stirred tank reactors (STRs)** play a central role in chemical process industry and biotechnology. A typical **STR** contains one or more impellers affixed to a shaft as well as baffles mounted to the reactor wall. A diverse set of parameters, including tank and impeller size, stirring rate, as well as the number of baffles, offer flexibility and control over the **STR's** performance. However, these factors also pose significant challenges in designing and scale-up (or scale-down) of

2020 *Mathematics Subject Classification.* Primary: 76-10, 68T07; Secondary: 76D05, 35Q68.

Key words and phrases. Physics-Informed Neural Networks, Domain Decomposition, Reduced Order Modeling, Navier-Stokes Equations, Stirred Tank Reactors.

Corresponding author: Veronika Trávníková.

*Equal contribution.

such reactors. Therefore, it is essential to understand the quantitative influence of these parameters on design objectives. As measurements are often prohibitively complicated, it is difficult to gain insight into the conditions inside these reactors. Models of **STRs** serve a dual purpose: They can help reduce the need for extensive experimental studies during process design and scale-up, while also enhancing our understanding of the conditions within the reactor. In industry, **Computational Fluid Dynamics (CFD)** is already widely employed for this task. Nevertheless, high-fidelity simulations come at a significant computational cost, particularly in scenarios where the same model needs to be evaluated repeatedly with different parameters.

An example of such a scenario is the application of **STRs** as bioreactors in bioprocesses. A bioreactor typically contains a suspension of cells that are fed nutrients and, in turn, catalyze metabolic processes to produce desired products, such as antibiotics or antibodies. When modeling bioprocesses, two fundamental phenomena come into play: the hydrodynamics, which pertains to the flow field inside the reactor, and the kinetics of the biochemical reaction. These phenomena are closely interconnected, as heterogeneities in nutrient concentration lead to variations in intra-cellular composition among cells. Cells move within the tank during mixing, and even two cells in the same location at a given time may exist in different states. Consequently, a fast-to-evaluate flow model is essential for coupling with the mass transfer model [14].

This challenge encourages the development of computationally efficient **Reduced Order Models (ROMs)** that can provide fast approximate solutions for process design. Recent advancements in deep learning have sparked interest in employing data-driven approaches to address this need, particularly due to the advantage of offline pretraining and subsequent quick model evaluation offered by **Machine Learning (ML)**. **ML** has been employed to construct **ROMs**, for example, by utilizing autoencoders – artificial neural networks that learn the mapping from high-dimensional input to a low-dimensional space [46]. However, acquiring a sufficiently large training dataset for our specific application case proves prohibitively costly. Consequently, we aim to leverage our insights into the underlying physics of the problem to reduce or potentially eliminate the need for training data.

Physics-Informed Neural Networks (PINNs) integrate the governing equations of the problem into the loss function of the **Neural Network (NN)**, making them a natural fit for our objectives. Since the seminal paper of Raissi et al. (2019) [31], **PINNs** have been successfully applied to problems across diverse domains, including solid mechanics [24, 13, 34], molecular dynamics [15], chemical reaction kinetics [2], the wave equation [28], hemodynamics [21, 38, 32], cardiac activation mapping [35], and various other fields [7]. Furthermore, **PINNs** have been applied to address numerous problems in fluid mechanics [19, 6, 18, 40, 12, 47]. Notably, they have been employed to reconstruct the 3D wake flow past a cylinder using data from a few cross-planes [5] or as closure for **Reynolds-Averaged Navier-Stokes (RANS)** equations [11]. The approach presented in this paper extends beyond embedding the governing equations into the model training. We incorporate additional insights by implementing strong **boundary conditions (BCs)** [36] with a lifting function, aligned with an estimated velocity profile. Additionally, we perform **domain decomposition (DD)**, solving different sets of equations in different subdomains according to the distinct flow characteristics present in each respective region.

The rest of the paper is structured as follows: Section 2 briefly introduces the reader to the mathematical basics of NNs and PINNs. Since the field of PINNs is rapidly evolving, we will only focus on presenting the developments that are of immediate relevance to our work such as Extended Physics-Informed Neural Networks (XPINNs) and strong BC imposition. After that, we present the application to which we are employing our method in Section 3. We explain the model problem that we will consider in this paper in detail, which includes stating our assumptions, the fundamental physical conservation laws that govern the flow in the STR and the employed BCs. We conclude the theory part of the paper by elaborating on the validation strategy for the PINN models. The following Sections 4 and 5 then contain the main findings of this work. We start with presenting a model hierarchy for a simpler case, where we only train PINNs to predict the flow field for one fixed Reynolds number in Section 4. Here, we detail how we successively tested different approaches to increase the predictive accuracy of the reduced simulation models. Since we are interested in reliable ROMs for multi-query scenarios, we then transfer these findings in Section 5 to predict the flow field inside our STR geometry for different impeller velocities. Finally, Section 6 concludes this work by summarizing the main results and providing an outlook on future work.

2. Methods. In this section, we briefly outline the basics of the methods applied in this paper. Consequently, we first recapitulate the mathematical definition of a fully-connected feed-forward NN — the NN architecture to which we restrict ourselves within this paper — before we introduce our PINN-related notation. To keep both sections concise, we will only mention the aspects that are most important for this paper and refer to the literature for a more in-depth discussion of the respective methods.

2.1. Fully-connected feed-forward NNs. In this work, we only consider fully-connected feed-forward NNs, that is, every neuron of the preceding layer is connected to every neuron of the following layer and all connections are directed forward, i.e., information is only passed from one layer onward to the next. Mathematically, a NN mapping from an input space \mathcal{X} to an output space \mathcal{U} and consisting of N_L layers can be formalized as

$$\mathcal{NN} : \mathcal{X} \rightarrow \mathcal{U}, \mathbf{x} \mapsto \mathcal{NN}(\mathbf{x}; \boldsymbol{\theta}) = \left(\mathbf{f}^{(N_L)} \circ \dots \circ \mathbf{f}^{(1)} \right) (\mathbf{x}; \boldsymbol{\theta}), \quad (1)$$

where each layer is described by a function

$$\mathbf{f}^{(l)}(\mathbf{x}; \boldsymbol{\theta}^{(l)}) = \sigma^{(l)}(\mathbf{W}^{(l)}\mathbf{x} + \mathbf{b}^{(l)}) \quad \forall l \in \{1, \dots, N_L\}. \quad (2)$$

Here, $\boldsymbol{\theta}^{(l)} = \{\mathbf{W}^{(l)}, \mathbf{b}^{(l)}\}$ denotes the trainable parameters, namely the layer's weights and biases, while σ denotes the activation function acting element-wise on its input. In principle, one can employ different activation functions after every layer. For the rest of this paper, however, we restrict ourselves to the same activation after all hidden layers and a linear activation function in the last layer, that is $\sigma^{(l)}(\mathbf{z}) = \sigma(\mathbf{z}) \forall l \in \{1, \dots, N_{L-1}\}$ and $\sigma^{(N_L)}(\mathbf{z}) = \mathbf{z}$. For the complete network as defined in Equation (1), $\boldsymbol{\theta} = \{\boldsymbol{\theta}^{(1)}, \dots, \boldsymbol{\theta}^{(N_L)}\}$ denotes the collection of layer-wise parameters and $\mathbf{x} \in \mathcal{X}$ the input vector.

In the following, we will employ fully-connected feed-forward NNs only for regression tasks, i.e., $\mathcal{X} \subseteq \mathbb{R}^{N_{\text{in}}}$ and $\mathcal{U} \subseteq \mathbb{R}^{N_{\text{out}}}$.

2.2. Physics-Informed Neural Networks (PINNs). The concept of PINNs was already proposed in the last century [23, 30] but received again attention in recent years [31] after the advances in computational resources and broad availability of efficient algorithmic differentiation implementations made the approach more viable. The basic idea of PINNs is to let a NN (e.g., as introduced in Equation (1)) approximate the unknown solution field of a (partial) differential equation. Let us consider the following generic formulation of a **partial differential equation (PDE)** (system)

$$\mathcal{R}[\mathbf{u}] = \mathbf{0} \quad \text{in } \Omega, \quad (3a)$$

$$\mathcal{B}[\mathbf{u}] = \mathbf{0} \quad \text{on } \Gamma, \quad (3b)$$

where $\mathcal{R}[\cdot]$ denotes the **PDE** and $\mathcal{B}[\cdot]$ the **initial and boundary condition (IBC)** operator, both formulated as residuals. In the general case of **PDE** systems, $\mathcal{R}[\cdot]$ and $\mathcal{B}[\cdot]$ are usually vectors. \mathbf{u} corresponds to the (unknown) **PDE** solution which will now be approximated by a **NN**

$$\mathbf{u}(\mathbf{x}) \approx \mathbf{u}_\theta(\mathbf{x}) := \mathcal{NN}(\mathbf{x}; \theta). \quad (4)$$

During training, this **NN** first predicts the approximated **PDE** solution at (randomly) selected points of the domain Ω and the boundary $\Gamma = \partial\Omega$. The deviation from the true solution is then subsequently quantified by evaluating the residuals of Equation (3) on these predictions. This yields the following *physics-informed* loss function for the training:

$$\mathcal{L}_{\text{phys}}^{\text{PINN}}(\theta; \mathbf{X}) = \alpha_{\text{PDE}} \cdot \mathcal{L}_{\text{PDE}}(\theta; \mathbf{X}_{\text{PDE}}) + \alpha_{\text{IBC}} \cdot \mathcal{L}_{\text{IBC}}(\theta; \mathbf{X}_{\text{IBC}}), \quad (5a)$$

with

$$\mathcal{L}_{\text{PDE}}(\theta; \mathbf{X}_{\text{PDE}}) = \frac{1}{N_{\text{PDE}}} \sum_{i=1}^{N_{\text{PDE}}} \left(\mathcal{R} \left[\mathbf{u}_\theta \left(\mathbf{x}_{\text{PDE}}^{(i)} \right) \right] \right)^2, \quad (5b)$$

$$\mathcal{L}_{\text{IBC}}(\theta; \mathbf{X}_{\text{IBC}}) = \frac{1}{N_{\text{IBC}}} \sum_{i=1}^{N_{\text{IBC}}} \left(\mathcal{B} \left[\mathbf{u}_\theta \left(\mathbf{x}_{\text{IBC}}^{(i)} \right) \right] \right)^2. \quad (5c)$$

In the case of vector-valued operators $\mathcal{R}[\cdot]$ and $\mathcal{B}[\cdot]$, the square operation in our notation is to be understood component-wise so that \mathcal{L}_{PDE} and \mathcal{L}_{IBC} are again vectors. Moreover, $\mathbf{X} = \{\mathbf{X}_{\text{PDE}}, \mathbf{X}_{\text{IBC}}\}$ denotes the set of evaluation points — also referred to as *collocation points* — on which the **PDE** as well as the (initial and) **BCs** are evaluated. $\mathbf{X}_{\text{PDE}} = \{\mathbf{x}_{\text{PDE}}^{(1)}, \dots, \mathbf{x}_{\text{PDE}}^{(N_{\text{PDE}})}\}$ and $\mathbf{X}_{\text{IBC}} = \{\mathbf{x}_{\text{IBC}}^{(1)}, \dots, \mathbf{x}_{\text{IBC}}^{(N_{\text{IBC}})}\}$ represent the collocation points in the domain and on the boundary respectively. α_{PDE} and α_{IBC} are scaling factors that allow to weigh the individual contributions of the physical constraints differently.

Selecting appropriate loss scaling factors. A great deal of research has been dedicated to the choice of these scaling factors, as they have been found to severely impact the convergence of the training as well as the accuracy of the prediction of PINNs [44]. Several methods have been proposed to choose these scaling factors appropriately. Most of these methods involve dynamic updates during training. For linear and well-posed **PDE** problems, van der Meer et al. (2022) [41] derived optimal loss scaling factors. However, that requires an analytical solution which is usually not available in engineering applications. In addition, they proposed a heuristic that alleviates this requirement. In [25], Li et al. (2022) proposed a bi-level optimization algorithm where the loss scales are adapted by gradient descent steps.

Another method to adapt the loss scales was proposed by Wang et al. (2021) [44], which is based on the magnitude of the gradients of the loss components. In their follow-up work [45], they proposed another update mechanism, leveraging insights from neural tangent kernel theory.

A remark about data. Although the general idea of PINNs is to overcome the need for training data — which is often scarce in engineering applications — available data can be integrated into the framework presented above. To that end, Equation (5a) can be modified as follows:

$$\mathcal{L}_{\text{phys+data}}^{\text{PINN}}(\boldsymbol{\theta}; \mathbf{X}) = \mathcal{L}_{\text{phys}}^{\text{PINN}}(\boldsymbol{\theta}; \{\mathbf{X}_{\text{PDE}}, \mathbf{X}_{\text{IBC}}\}) + \alpha_{\text{data}} \cdot \mathcal{L}_{\text{data}}(\boldsymbol{\theta}; \mathbf{X}_{\text{data}}), \quad (6a)$$

where

$$\mathcal{L}_{\text{data}}(\boldsymbol{\theta}; \mathbf{X}_{\text{data}}) = \frac{1}{N_{\text{data}}} \sum_{i=1}^{N_{\text{data}}} \left(\mathbf{u}_{\boldsymbol{\theta}} \left(\mathbf{x}_{\text{data}}^{(i)} \right) - \mathbf{u}_{\text{data}}^{(i)} \right)^2. \quad (6b)$$

Here, $\mathbf{X}_{\text{data}} = \left\{ \left(\mathbf{x}_{\text{data}}^{(1)}, \mathbf{u}_{\text{data}}^{(1)} \right), \dots, \left(\mathbf{x}_{\text{data}}^{(N_{\text{data}})}, \mathbf{u}_{\text{data}}^{(N_{\text{data}})} \right) \right\}$ represents a training set with high-fidelity information on the solution $\mathbf{u}_{\text{data}}^{(i)}$ at input locations $\mathbf{x}_{\text{data}}^{(i)}$.

2.3. Advanced PINN architectures. The preceding section covered the fundamental PINN architecture. Nevertheless, at the time of writing, a variety of more complex architectures have been proposed [17, 20, 27, 29, 44], which have been tailored to overcome known drawbacks of PINNs or to improve the predictive capabilities beyond those of plain baseline PINNs. Due to their relevance for the work of this paper, we will briefly outline the idea of XPINNs [16] in the following. In the literature, a similar approach has been reported under the name **Distributed Physics-Informed Neural Networks (DPINNs)** [10].

The general idea is motivated by DD approaches: The computational domain Ω is decomposed into N_d non-overlapping subdomains Ω_k such that $\bigcup_{k=1}^{N_d} \Omega_k = \Omega$, with $\Omega_i \cap \Omega_j = \Gamma_{ij} \forall i, j \leq N_d \wedge i \neq j$. Within each of these subdomains Ω_k , a different PINN $\mathbf{u}_{\boldsymbol{\theta}^{(k)}}$ is trained. This approach allows to adapt the architecture of the network to the structure of the solution: In regions of the domain where smooth solutions are expected, the networks can be narrower and shallower, while deeper and wider network architectures might be required in regions where the solution is more complex. The complete PDE solution is then assembled from the individual sub-networks' predictions in their specific regions, that is,

$$\mathbf{u}_{\boldsymbol{\theta}}(\mathbf{x}) = \sum_{k=1}^{N_d} \mathbf{u}_{\boldsymbol{\theta}^{(k)}}(\mathbf{x}) \mathbb{I}_{\Omega_k}(\mathbf{x}), \quad (7)$$

with the indicator function

$$\mathbb{I}_{\Omega_k}(\mathbf{x}) = \begin{cases} 1 & \mathbf{x} \in \Omega_k \setminus \Gamma_k \\ \frac{1}{2} & \mathbf{x} \in \Gamma_k \\ 0 & \mathbf{x} \notin \Omega_k \end{cases}. \quad (8)$$

All networks are trained simultaneously. Efficient methods for parallelizing the training of the N_d networks have been proposed, e.g., in [37]. The predictions of the different sub-networks are coupled by augmenting Equation (5a) with additional terms representing the equality of the residuals and average values across sub-domain boundaries as well as continuity constraints on the solution values and their derivatives (if needed).

2.4. Input and output scaling. For all models presented in Sections 4 and 5, we normalize inputs and outputs to improve the learning process. Essentially, we non-dimensionalize inputs and outputs as suggested in literature [43] by adding fixed (i.e., not learned) feature transformation layers to the network that transform the inputs to be roughly contained in the interval $[-1, 1]^{N_{\text{in}}}$ and rescale the outputs from $[-1, 1]^{N_{\text{out}}}$ to the actual dimensional quantities. Mathematically, we augment Equation (4) by additionally composing it with a pre-processing function \mathbf{f}_{pre} and a post-processing function \mathbf{f}_{post} , so that

$$\mathbf{u}_{\theta}(\mathbf{x}) = \mathbf{f}_{\text{post}}(\mathbf{x}) \circ \mathcal{NN}(\mathbf{x}; \theta) \circ \mathbf{f}_{\text{pre}}(\mathbf{x}). \quad (9)$$

The pre- and post-processing functions employed in our work differ among the different models and will be reported in the respective sections.

2.5. Strong imposition of Dirichlet BCs. So far, in the previous sections we have only discussed the case where the BCs of the PDE problem Equation (3) are enforced weakly, that is, via a penalty term in the loss function (c.f. Equation (5c)). However, research has been dedicated to imposing Dirichlet BCs of the form $\mathbf{u}(\mathbf{x}) = \mathbf{h}(\mathbf{x})$ on Γ_D strongly, similar to what is often done in the Finite Element Method (FEM). Mathematically, the strong imposition of Dirichlet boundaries takes the form of a post-processing operation, as discussed in the previous section, i.e., the ansatz Equation (4) is modified as follows:

$$\mathbf{u}_{\theta}(\mathbf{x}) = \mathbf{h}(\mathbf{x}) + \mathbf{g}(\mathbf{x}) \odot \mathcal{NN}(\mathbf{x}; \theta), \quad (10)$$

where $\mathbf{h}(\mathbf{x})$ is the (known) Dirichlet BC on the Dirichlet part of the boundary $\Gamma_D \subseteq \Gamma$ and $\mathbf{g}(\mathbf{x})$ a function that depends on the geometry of the computational domain Ω with the properties

$$\begin{cases} \mathbf{g}(\mathbf{x}) = \mathbf{0} & \text{on } \Gamma_D \\ \mathbf{g}(\mathbf{x}) > \mathbf{0} & \text{in } \Omega \setminus \Gamma_D \end{cases}. \quad (11)$$

The symbol \odot in Equation (10) symbolizes the component-wise multiplication of two vectors.

In the literature, different approaches have been proposed of how to construct the positive semi-definite function \mathbf{g} which vanishes on the Dirichlet boundary. For simple rectangular geometries, Lagari et al. (2020) [22] describe a construction using polynomials and exponential functions that generalizes to arbitrary dimensions and can also be applied to Neumann and Robin conditions. For more complex geometries, an algorithm has been proposed in [36] that constructs \mathbf{g} through a radial-basis function interpolation of point samples generated on the domain boundary.

3. Model. In this section, we introduce the simulation model that serves as the basis for the construction of the corresponding PINN-based ROMs proposed in this paper. We discuss the governing equations and explain the test case that will be investigated in the following Sections 4 and 5 before briefly commenting on the classical numerical solution approach via the FEM which we used to generate the validation results for our models.

3.1. Assumptions. As mentioned in the introduction, modeling the flow field inside STRs poses a number of challenges. For developing PINN-based ROMs, we consequently make some simplifying assumptions to reduce the complexity of the learning task, especially since we are interested in approaches that learn solutions of reasonable accuracy without the help of high-fidelity data. Therefore, we assume

- an incompressible, Newtonian fluid, i.e., the density ρ and viscosity μ are constant,
- a single phase flow, i.e., we neglect inhomogeneities inside the vessel,
- and a steady flow, i.e., we are only interested in finding the solution for the flow field at a specific instance in time.

The last simplification enables us to circumvent the complexities associated with the moving domain that would arise from a rotating stirrer. While these simplifications shift the model away from realistic applications such as bioreactors, they allow us to conduct a feasibility study and identify the most promising methodologies. Moving forward, our aim is to apply these methodologies to models with increased complexity and explore more realistic scenarios.

Before we introduce the problem domain Ω that will be considered throughout Sections 4 and 5, we first briefly state the governing equations resulting from the assumptions above.

3.2. Governing equations. The mass and momentum balance inside the problem domain are given by the stationary, incompressible Navier-Stokes equations. The total PDE residual in Equation (5b) consists of the following components $\mathcal{R}[\mathbf{u}] = (\mathcal{R}_{\text{momentum}}[\mathbf{u}]^T, \mathcal{R}_{\text{mass}}[\mathbf{u}]^T)^T$. We solve these for the unknown velocity vector $\mathbf{v} = (v_x, v_y)^T$ and the unknown pressure p , i.e., $\mathbf{u} = (\mathbf{v}^T, p)^T$. The residuals of the mass and momentum balance are given by

$$\mathcal{R}_{\text{momentum}}[\mathbf{u}] = \rho(\mathbf{v} \cdot \nabla)\mathbf{v} + \nabla p - \mu\Delta\mathbf{v} , \quad (12a)$$

$$\mathcal{R}_{\text{mass}}[\mathbf{u}] = \nabla \cdot \mathbf{v} . \quad (12b)$$

These conservation laws need to be equipped with suitable BCs that depend on the problem domain, which we will introduce next.

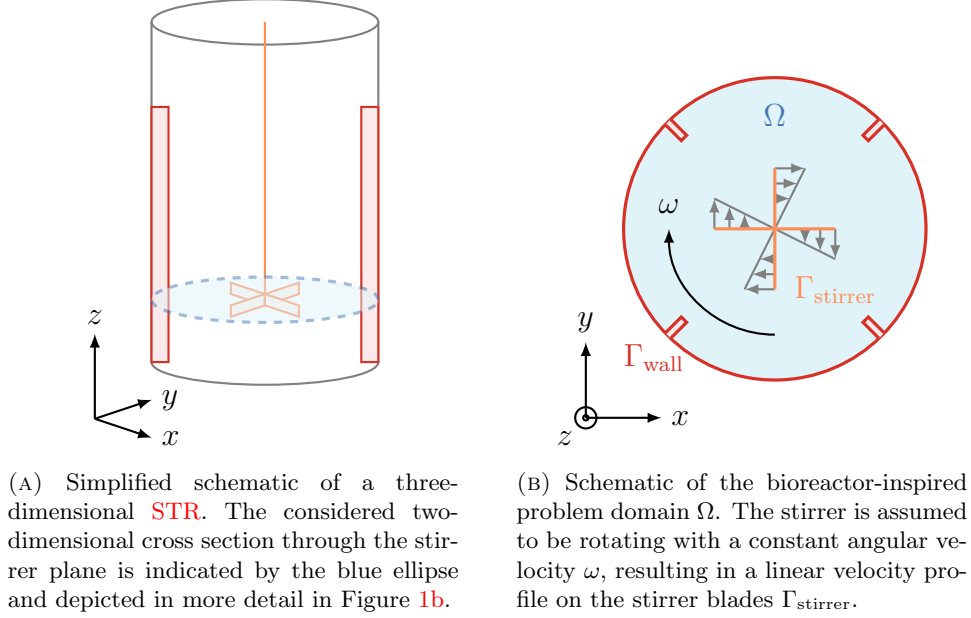
3.3. Problem domain and boundary conditions. As modeling the flow inside a realistic three-dimensional geometry is a challenging task and the focus of this paper is on laying the ground-work by identifying promising methodologies to be translated into the development of a ROM for more realistic scenarios, we first consider the planar flow in a two-dimensional cross section through the stirrer plane (see Figure 1a). The resulting computational domain is depicted in Figure 1b.

This choice of the computational domain can be understood as follows: Our frame of reference is fixed and aligned with the Cartesian coordinate axes, whose origin is the center of the domain (see also Figure 2a). We train a model which predicts the flow field at the specific instance in time when the stirrer blades are exactly aligned with the x and y axes. As the stirrer is assumed to rotate with a constant angular velocity ω , a linear velocity profile develops on the stirrer blades according to the law of uniform circular motion. This results in the following BCs: Due to the no-slip condition, the fluid adheres to the stirrer on Γ_{stirrer} , i.e., $\mathbf{v} = \mathbf{v}_{\text{stirrer}}$, where $\mathbf{v}_{\text{stirrer}}$ can be computed as

$$\mathbf{v}_{\text{stirrer}} = \boldsymbol{\omega} \times \mathbf{r} , \quad (13)$$

where $\boldsymbol{\omega}$ is the rotational velocity vector and \mathbf{r} the radial vector originating from the center of rotation. In 2D, only rotation around the z -axis is possible, i.e., $\boldsymbol{\omega} = \omega\mathbf{e}_z$, with \mathbf{e}_z denoting the unit vector in z -direction. Consequently, Equation (13) simplifies to

$$\mathbf{v}_{\text{stirrer}} = \begin{pmatrix} \omega y \\ -\omega x \end{pmatrix} , \quad (14)$$



(A) Simplified schematic of a three-dimensional **STR**. The considered two-dimensional cross section through the stirrer plane is indicated by the blue ellipse and depicted in more detail in Figure 1b.

(B) Schematic of the bioreactor-inspired problem domain Ω . The stirrer is assumed to be rotating with a constant angular velocity ω , resulting in a linear velocity profile on the stirrer blades Γ_{stirrer} .

FIGURE 1. Schematic depiction of a three-dimensional **STR** geometry (A) as well as the simplified two-dimensional problem domain considered in the rest of this paper (B).

if the origin of the xy -coordinate system is located on the stirrer axis. On the reactor wall Γ_{wall} , we employ the no-slip condition, i.e., $\mathbf{v} = \mathbf{0}$.

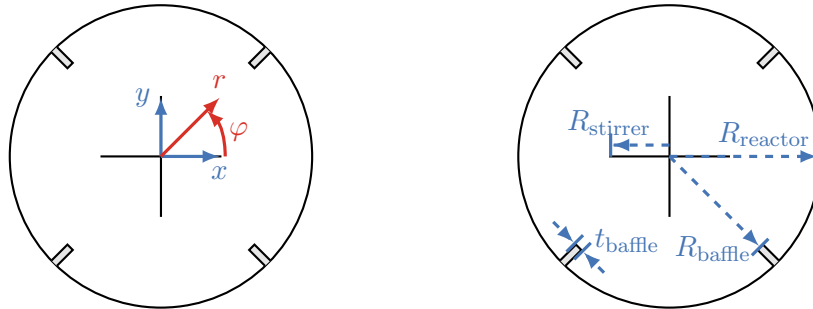
This allows us to define the following **BC** residuals that are required for the loss function of the **PINN** Equation (5c) as $\mathcal{B}[\mathbf{u}] = (\mathcal{B}_{\text{wall}}[\mathbf{u}]^T, \mathcal{B}_{\text{stirrer}}[\mathbf{u}]^T)^T$, with

$$\mathcal{B}_{\text{wall}}[\mathbf{u}] = \begin{pmatrix} v_x \\ v_y \end{pmatrix}, \quad (15a)$$

$$\mathcal{B}_{\text{stirrer}}[\mathbf{u}] = \begin{pmatrix} v_x - \omega y \\ v_y + \omega x \end{pmatrix}. \quad (15b)$$

For some models presented in Sections 4 and 5, we will consider the problem domain in polar instead of Cartesian coordinates. Both coordinate systems are visualized in Figure 2a. We will denote the Cartesian input vector by $\mathbf{x}_{\text{cart}} := (x, y)^T \in \Omega_{\text{cart}}$ and write $\mathbf{x}_{\text{polar}} := (r, \varphi)^T \in \Omega_{\text{polar}}$ in the case of polar coordinates. For the case of the parameterized model presented in Section 5, we only consider polar coordinates but extend the polar domain Ω_{polar} by the parameter space Λ . Consequently, we denote the input vector as $\mathbf{x}_{\text{param}} := (r, \varphi, \omega)^T \in \Omega_{\text{polar}} \times \Lambda$.

The geometry of our domain can be described by geometrical quantities visualized in Figure 2b. Their numerical values are listed in Table 1a. Table 1b lists the values for the density and viscosity which we consider constant throughout this work. Note that the stirrer velocity ω is not listed in either table. While we consider a fixed stirrer velocity in Section 4 corresponding to a Reynolds number of $\text{Re} = 4000$, in Section 5 we treat it as a variable parameter and train **PINNs** that can predict the flow field for different impeller speeds. The Reynolds number, which describes the ratio of inertial to viscous forces in a fluid, is an important non-dimensional



(A) Definition of Cartesian and polar coordinate systems for the problem domain.

(B) Geometrical dimensions of the problem domain.

FIGURE 2. Coordinate systems and geometrical dimensions related to the problem domain.

TABLE 1. Geometrical dimensions and material properties that are considered constant throughout the paper.

(A) Geometrical dimensions of the STR depicted in Figure 2b.

Quantity	Value [m]
R_{stirrer}	0.040
R_{baffle}	0.085
R_{reactor}	0.100
t_{baffle}	0.005

(B) Constant material properties used for the simulations and PINN training.

Property	Value	Unit
ρ	1000	kg/m ³
μ	0.001	kg/m s

quantity to characterize flow regimes. In this paper, we follow the definition from [33], i.e.,

$$\text{Re} = \frac{\rho\omega(2R_{\text{stirrer}})^2}{\mu}. \quad (16)$$

From Equation (16) we can see that the operating point of $\text{Re} = 4000$ corresponds to a stirrer velocity of $\omega = 0.625 \text{ rad/s}$.

3.4. Validation. The models trained within the scope of this paper were validated against reference solutions obtained from high-fidelity simulations using our in-house solver XNS [9]. The problem defined above was discretized on an unstructured mesh $\Omega_{\text{ref}} \subset \Omega$ consisting of 73,164 triangular elements and $N_{\text{ref}} = 37,117$ nodes and solved using a stabilized FEM approach [39] with linear basis functions for the pressure and velocity fields. High-fidelity solutions were obtained for $\text{Re} \in \{1000, 4000, 6000, 8000, 10,000\}$. Reference solutions for velocity and pressure for $\text{Re} = 4000$ are shown in Figure 3.

We used point-wise ℓ^1 and ℓ^2 errors as defined in Equation (19) as metrics to evaluate the performance of the models. Each trained PINN model was employed to make predictions for a randomly selected subset of $N_{\text{eval}} = 10,000$ nodes $\mathbf{X}_{\text{eval}} \subset \Omega_{\text{ref}}$ from the reference mesh. While we can directly compute the discrepancy between the predicted velocity field and the reference velocity, the pressure

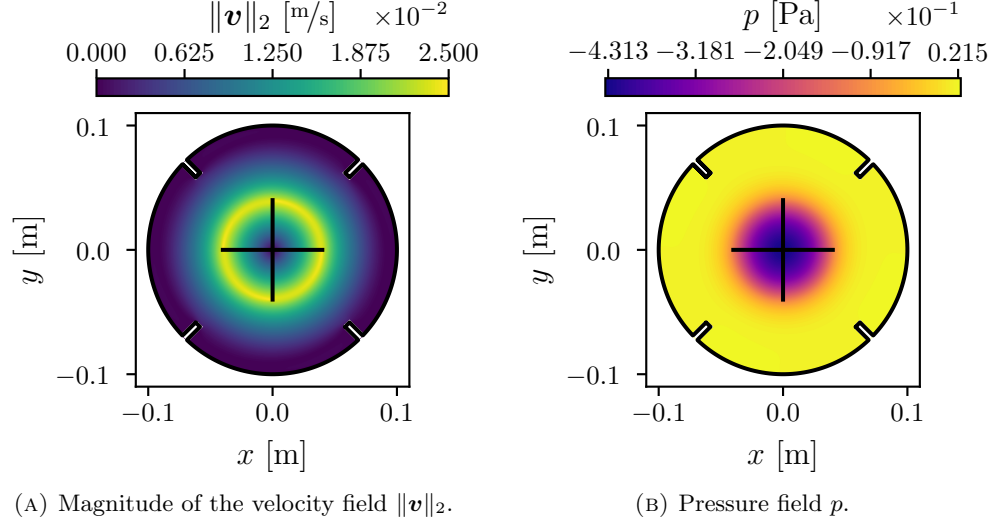


FIGURE 3. High-fidelity solution for velocity (A) and pressure (B) at $\text{Re} = 4000$ that was used to validate predictions of the PINN models.

predictions cannot be directly compared to the reference solution: Since our problem formulation does not constrain the pressure in the computational domain, we first need to ensure that the predicted pressure and reference values are on the same scale. To this end, we apply an affine transformation so that the pressure maximum is zero for both the PINN predictions and the reference solution, i.e.,

$$\tilde{p}^{\text{PINN}}(\mathbf{x}) = p^{\text{PINN}}(\mathbf{x}) - p_{\max}^{\text{PINN}}, \quad (17a)$$

$$\tilde{p}_{\mathbf{x}}^{\text{ref}} = p_{\mathbf{x}}^{\text{ref}} - p_{\max}^{\text{ref}}, \quad (17b)$$

with $p_{\max}^{(\cdot)} = \max_{\mathbf{x} \in \mathbf{X}_{\text{eval}}} p^{(\cdot)}$. Subsequently, we can define the point-wise error function for a quantity $q \in \{\tilde{p}, \mathbf{v}\}$ as

$$f_{\text{err}}^{(q)}(\mathbf{x}) = \|q^{\text{PINN}}(\mathbf{x})\|_2 - \|q_{\mathbf{x}}^{\text{ref}}\|_2. \quad (18)$$

Remark: In case of a vector-valued quantity, its 2-norm is defined as $\|q\|_2 := \sqrt{q_x^2 + q_y^2}$, while for a scalar quantity, the 2-norm is equivalent to the absolute value $\|q\|_2 \equiv |q|$.

With that, we compute the (normalized) ℓ^1 and ℓ^2 errors of our models as

$$\delta_{\ell^1}^{(q)} = \frac{1}{q_{\text{norm}}} \frac{1}{N_{\text{eval}}} \sum_{k=1}^{N_{\text{eval}}} \left| f_{\text{err}}^{(q)}(\mathbf{x}_k) \right|, \quad (19a)$$

$$\delta_{\ell^2}^{(q)} = \frac{1}{q_{\text{norm}}} \sqrt{\frac{1}{N_{\text{eval}}} \sum_{k=1}^{N_{\text{eval}}} \left(f_{\text{err}}^{(q)}(\mathbf{x}_k) \right)^2}. \quad (19b)$$

Here, q_{norm} stands for a normalizing quantity to which the errors are relative to. We use the velocity at the tip of the stirrer, $v_{\text{norm}} \equiv v_{\text{tip}} := \omega R_{\text{stirrer}}$, and the range

of reference pressure, $\tilde{p}_{\text{norm}} \equiv p_{\Delta}^{\text{ref}} := p_{\text{max}}^{\text{ref}} - p_{\text{min}}^{\text{ref}}$ as normalizing quantities for $\delta^{(v)}$ and $\delta^{(\tilde{p})}$, respectively.

4. Non-parameterized case. The initial stage of our work focused on exploring various strategies to improve the prediction quality of PINNs for our application. The non-parameterized models were trained for fixed $\text{Re} = 4000$. The best performing model identified in this section was then extended through the introduction of the rotational velocity of the stirrer as a parametric input. This section presents a series of PINN configurations, each increasing in complexity as we progressively incorporate insights into the physics of the problem into the model. Supplementary information for all models which is not explicitly commented on in the following sections can be found in the model-respective section in Appendix A.

4.1. Baseline model. In the most basic PINN configuration, the model is trained on the domain Ω_{cart} , with the input vector to the NN, \mathbf{x}_{cart} , consisting of Cartesian coordinate pairs for the training points. The loss function comprises the residuals of the conservation equations as defined in Equation (12) and BC residuals for Γ_{wall} and Γ_{stirrer} as defined in Equation (15). Scaling factors for all loss components are set to one. The pre-processing function \mathbf{f}_{pre} from Equation (9) is chosen as

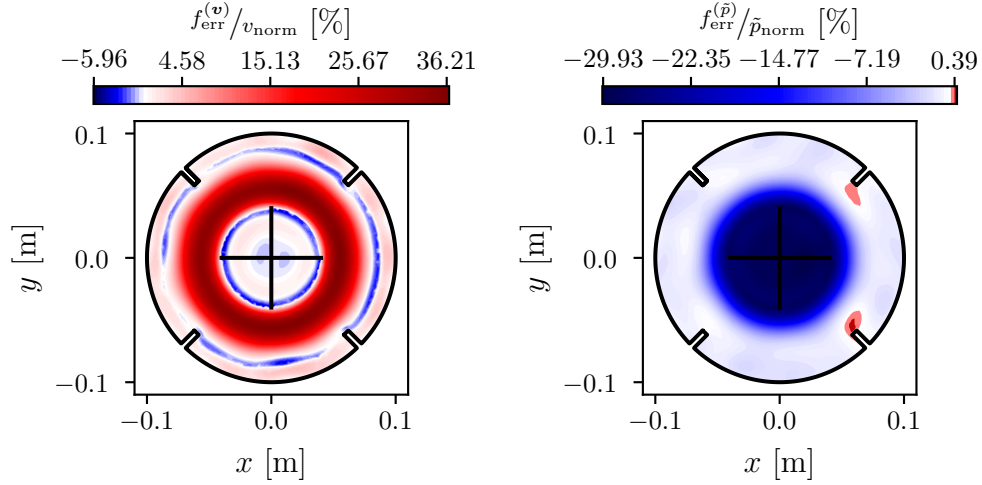
$$\tilde{\mathbf{x}} = \mathbf{f}_{\text{pre}}(\mathbf{x}_{\text{cart}}) = \begin{pmatrix} x/R_{\text{reactor}} \\ y/R_{\text{reactor}} \end{pmatrix}. \quad (20)$$

The non-dimensional outputs of the network are scaled as follows:

$$\mathbf{u} = \mathbf{f}_{\text{post}}(\tilde{\mathbf{u}}) = \begin{pmatrix} v_{\text{tip}} \tilde{v} \\ \rho v_{\text{tip}}^2 \tilde{p} \end{pmatrix}. \quad (21)$$

Figure 4 depicts the spatial distribution of the normalized velocity (Figure 4a) and pressure errors (Figure 4b). It is evident from Figure 4 that the baseline model struggles to accurately capture both the velocity and pressure fields, with the maximum normalized velocity error reaching approximately 36.2%. The pressure errors are most pronounced in the inner region around the stirrer ($r \lesssim R_{\text{stirrer}}$), while the errors in velocity magnitude are highest in the area between the stirrer and the baffles. In this region, the PINN relies solely on the PDE residuals without information from the labeled points on the boundary. In the further refinements of the model, we address this issue initially by incorporating labeled training data for the domain in Section 4.2 and subsequently by adjusting the scaling of the loss components corresponding to the PDE residuals in Section 4.3. Moreover, we observe that despite the symmetry of the problem domain, the learned solution lacks this property. We will address this shortcoming with a more advanced model in Section 4.4. As the accuracy in capturing the velocity field holds greater significance for our application than the pressure prediction, our focus will be on analyzing the velocity error and we will utilize it as the primary measure of model quality in the remainder of this paper.

4.2. Baseline model with data. Harnessing the ability of PINNs to integrate both physics and data losses (cf. Equation (6)), we introduce 2000 labeled training points obtained from the reference solution described in Section 3.4. Figure 5a illustrates that incorporating this additional information into the training notably enhances the predictive performance of the model detailed in Section 4.1. This improvement is evident in the reduction of both the maximum and average velocity error values, particularly in the domain far away from the boundaries. Nevertheless,



(A) Normalized error in velocity magnitude.

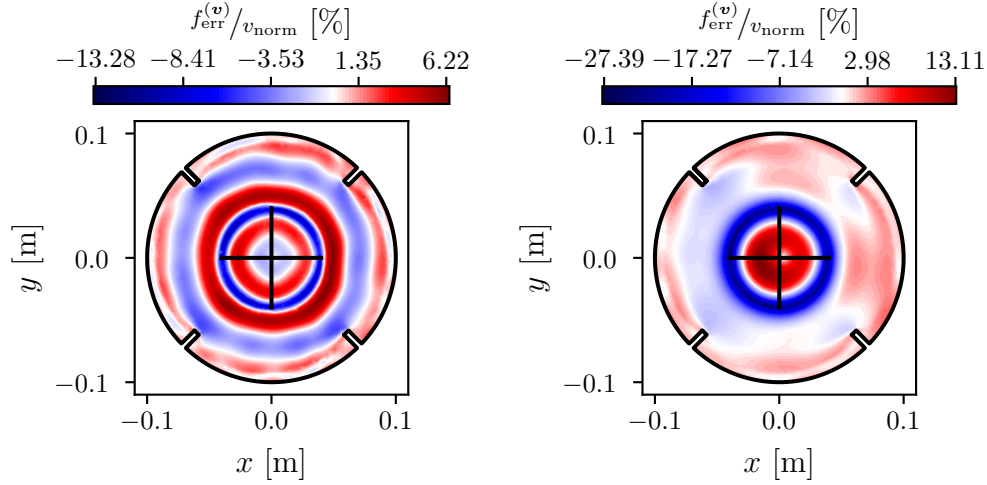
(B) Normalized error in pressure.

FIGURE 4. Spatial distribution of normalized errors of the baseline model presented in Section 4.1 for the velocity (A) and pressure fields (B). The velocity errors are most pronounced in the area between the stirrer and the baffles, where the PINN solely relies on the PDE residuals without information from the labeled boundary points, while the highest pressure errors are localized in the inner region around the stirrer.

it is reasonable to assume that acquiring such a substantial amount of data for each distinct set of process parameters would be prohibitively costly. Therefore, throughout the remainder of this section, we will focus on investigating strategies aimed at improving the performance of the model without the need for labeled data.

4.3. Baseline model with loss scaling. As mentioned in Section 2.2, the prediction capabilities of a PINN can be significantly improved by scaling the loss components appropriately. In this work, the scaling factors were manually tuned based on insights gained from the reference solution. As depicted in Figure 4a, utilizing unit scaling for the loss components results in a relatively low velocity error near Γ_{stirrer} , a slightly larger error near Γ_{wall} , while the most significant errors are observed further away from the boundaries. Based on this observation, we increase the scaling factors of $\alpha_{\text{PDE}} = (\alpha_{\text{momentum}_x}, \alpha_{\text{momentum}_y}, \alpha_{\text{mass}})^T$ to $(50, 50, 50)^T$ and set $\alpha_{\text{wall}} := 5$. Figure 5b shows that just by scaling the loss components we were able to significantly improve the accuracy of the velocity predicted by the PINN. The error for predictions within the domain between the stirrer tip and the wall now ranges from 5% to 10%, compared to over 30% observed with unit scaling in Section 4.1. The highest error is currently localized around the stirrer, as the loss component corresponding to the stirrer BC carries the least weight.

4.4. Baseline model in polar coordinates. Due to the geometry of the cross-section depicted in Figure 1b, polar coordinates are the more intuitive coordinate



(A) Normalized error in velocity magnitude of vanilla model with labeled data.

(B) Normalized error in velocity magnitude of baseline model with scaled loss components.

FIGURE 5. Spatial distribution of normalized velocity errors of the baseline model with labeled training data (A) and of the baseline model with scaled loss components (B).

system for the current application. Consequently, instead of solving for velocities in x - and y -direction $\mathbf{v}_{\text{cart}} = (v_x, v_y)^T$, we solve for the radial and circumferential velocity components $\mathbf{v}_{\text{polar}} = (v_r, v_\varphi)^T$. We can also leverage the fact that the geometry is symmetric to reduce the computational domain to $\Omega_{\text{sym}} \subset \Omega_{\text{polar}}$ depicted in Figure 7a, which constitutes a quarter of the original domain. The bounds of Ω_{sym} are defined by the axes connecting the opposing baffles. The input coordinates $\mathbf{x}_{\text{polar}}$ are then normalized such that

$$\tilde{\mathbf{x}} = \mathbf{f}_{\text{pre}}(\mathbf{x}_{\text{polar}}) = \begin{pmatrix} (r - R_{\text{stirrer}})/(R_{\text{reactor}} - R_{\text{stirrer}}) \\ 4\varphi/\pi \end{pmatrix}. \quad (22)$$

The respective outputs of the NN are scaled as

$$\mathbf{u} = \mathbf{f}_{\text{post}}(\tilde{\mathbf{u}}) = \begin{pmatrix} v_{r,\text{max}}^{\text{ref}} \tilde{v}_r \\ v_{\text{tip}} \tilde{v}_\varphi \\ \rho v_{\text{tip}}^2 \tilde{p} \end{pmatrix}, \quad (23)$$

where $v_{r,\text{max}}^{\text{ref}} = 8 \times 10^{-4}$ m/s was obtained from the high-fidelity solution on our reference mesh. The solution in the full domain can then be inferred from the solution in Ω_{sym} through projection onto the remaining part of the domain. We define the additional BC to ensure continuity of the solution on Γ_{sym} as:

$$\mathbf{u}|_{\mathbf{x}^{(+)}} = \mathbf{u}|_{\mathbf{x}^{(-)}} \quad \text{on } \Gamma_{\text{sym}}. \quad (24)$$

Here, $\mathbf{x}^{(+)}$ and $\mathbf{x}^{(-)}$ represent the left and right limiting values of spatial coordinates approaching Γ_{sym} .

Figure 6 demonstrates that in terms of average velocity prediction error, the model at hand performs similarly to the model presented in Section 4.3. Consequently, we can conclude that the choice of the coordinate system does not have

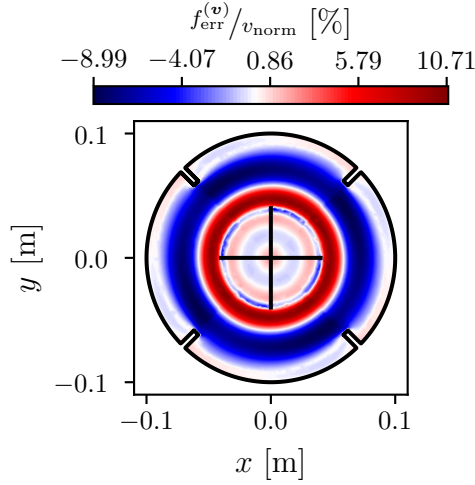
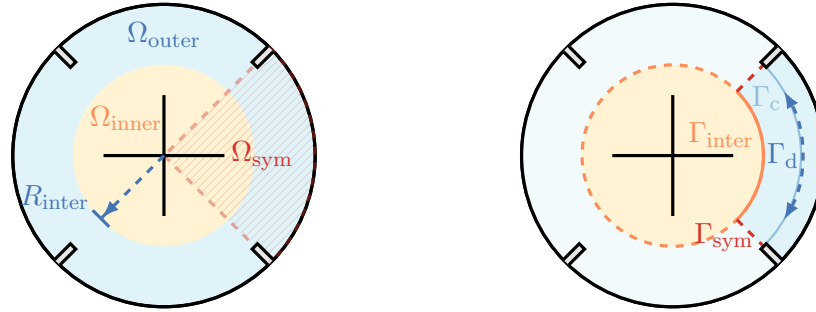


FIGURE 6. Spatial distribution of normalized error in velocity magnitude of the vanilla model trained on Ω_{sym} using polar coordinates.



(A) Division of the computational domain into an inner $\Omega_{\text{inner}} \subset \Omega_{\text{polar}}$ and outer region $\Omega_{\text{outer}} \subset \Omega_{\text{polar}}$. The interface between these two domains is located at $r = R_{\text{inter}}$. If a model exploits symmetry, only a quarter $\Omega_{\text{sym}} \subset \Omega_{\text{polar}}$ of the full domain Ω_{polar} is considered.

(B) Relevant interfaces used in the **DD** models. Γ_{inter} represents the interface between the inner and the outer domain, on Γ_c only the continuity of values is imposed while Γ_d additionally considers the continuity of derivatives. Γ_{sym} corresponds to the interface of the symmetry domain Ω_{sym} .

FIGURE 7. Schematic representation of the different subdomains and interfaces used in the more complex **PINN** configurations.

a significant impact on the predictive capabilities. It is also evident from Figure 6 that the symmetry boundary constraint is not entirely satisfied. This aspect could be further improved by fine-tuning the respective loss scaling factors.

4.5. Strong BC model. In all the models presented thus far, the most significant errors are localized near the tip of the stirrer and in its close proximity. A closer inspection of the velocity profiles along the radius of the domain for $\varphi = 0$, compared to the reference solution in Figure 8, indicates that the error stems from the inability

of the PINN to capture the sharp kink at the stirrer’s tip $r = R_{\text{stirrer}}$. Consequently, the Dirichlet BC at Γ_{stirrer} is violated. To address this issue and to reproduce

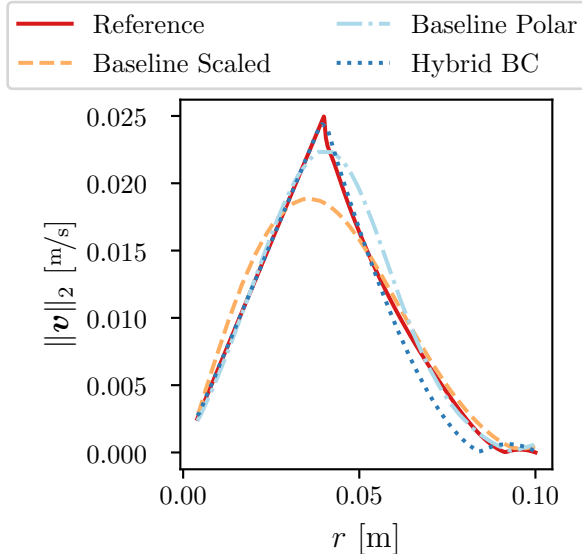
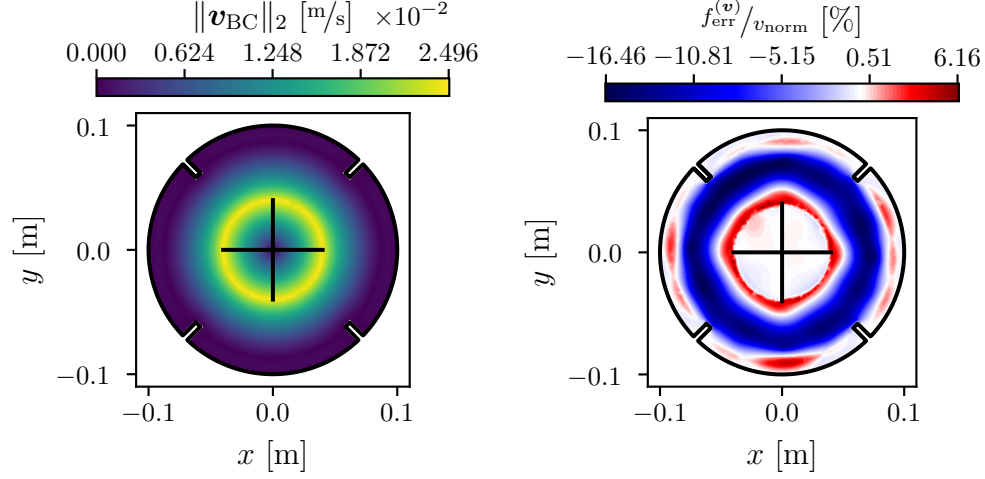


FIGURE 8. Velocity magnitudes of baseline models in radial direction for $\varphi = 0$. These models fail to capture the kink in velocity magnitude at the tip of the stirrer. This shortcoming is addressed by enforcing the Dirichlet BC at Γ_{stirrer} in a strong manner in Sections 4.5 and 4.6.

the kink more accurately, we explore the application of strong BCs as defined in Section 2.5. To impose the BCs for the velocity defined in Equation (15) in a strong manner through Equation (10), we construct the function $\mathbf{g}_{\text{strong}}$ using the approach outlined in [36] such that

$$\begin{cases} \mathbf{g}_{\text{strong}}(\mathbf{x}) = 0 & \text{on } \Gamma_{\text{stirrer}} \cup \Gamma_{\text{wall}} \\ 0 < \mathbf{g}_{\text{strong}}(\mathbf{x}) \leq 1 & \text{in } \Omega \setminus (\Gamma_{\text{stirrer}} \cup \Gamma_{\text{wall}}) . \end{cases} \quad (25)$$

Since the Dirichlet BCs only apply to velocity, the boundary value function from Equation (10) is defined as $\mathbf{h}(\mathbf{x}) := \mathbf{v}_{\text{BC}}$. Contrary to the findings reported in [36], our research indicates that the predictive capability of the model is influenced by the choice of \mathbf{h} . Hence, we attempt to employ a \mathbf{v}_{BC} that approximates the physical behavior to a certain extent. The selected function is illustrated in Figure 9a and its derivation is provided in Appendix C. In this model, the input normalization and output scaling outlined in Section 4.1 were employed. The post-processing function defined by Equation (10) was only applied to the velocity predictions after the outputs of the NN had been rescaled. We can observe from Figure 9b that the strong imposition of the BC on Γ_{stirrer} significantly aids in reducing the velocity prediction error around the stirrer. However, the error near Γ_{wall} and at the baffles is high. This could be attributed to the underlying boundary function \mathbf{v}_{BC} not accurately representing the solution in this region. In the following section, we



(A) Magnitude of the analytical function \mathbf{v}_{BC} used as \mathbf{h} in Equation (10) for strong imposition of BCs.

(B) Spatial distribution of normalized error in velocity magnitude for the model using strong imposition of Dirichlet BCs presented in Section 4.5. The error in velocity prediction around the stirrer is reduced, while the error near the wall and the baffles is high.

FIGURE 9. Analytical function satisfying the Dirichlet BCs in the domain (A) and spatial distribution of the normalized error of the model with strongly enforced BCs (B).

tackle this issue by maintaining strong BC imposition for the stirrer while reverting to soft BCs for the wall.

4.6. Hybrid BC model. To achieve better prediction capabilities and mitigate high errors in the region adjacent to the reactor wall, we choose to impose the BC on Γ_{stirrer} in a strong manner and utilize a soft BC imposition on Γ_{wall} . For this purpose, we define $\mathbf{g}_{\text{hybrid}}$ such that

$$\begin{cases} \mathbf{g}_{\text{hybrid}}(\mathbf{x}) = 0 & \text{on } \Gamma_{\text{stirrer}} \\ 0 < \mathbf{g}_{\text{hybrid}}(\mathbf{x}) \leq 1 & \text{in } \Omega \setminus \Gamma_{\text{stirrer}} \end{cases} \quad (26)$$

As demonstrated in Figure 10, this approach effectively reduces the overall error compared to the models presented thus far. Figure 8 illustrates that imposing strong BC on Γ_{stirrer} helps to capture the kink in the velocity profile accurately. The strong imposition of BCs also reduces the number of loss components that need scaling, consequently decreasing the number of hyperparameters requiring optimization. It is worth noting, however, that this comes at the expense of a significantly increased training time, as we will later discuss in Table 2 in Section 4.11.

4.7. Domain decomposition (DD) model. To further refine the model and improve the quality of the predictions, we can integrate additional insights from the reference solution. Notably, we observe minimal changes in both velocity and pressure in the circumferential direction within an inner region around the stirrer,

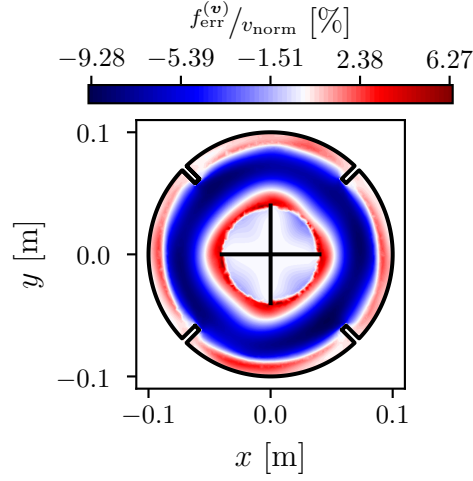


FIGURE 10. Spatial distribution of normalized error in velocity magnitude predicted by the model using hybrid imposition of Dirichlet BCs described in Section 4.6.

denoted by Ω_{inner} in Figure 7a. Additionally, the magnitude of the circumferential velocity significantly exceeds that of the radial velocity component, i.e.,

$$\frac{\partial(\cdot)}{\partial\varphi} = 0 \quad \wedge \quad v_\varphi \gg v_r \quad \text{in } \Omega_{\text{inner}} . \quad (27)$$

The governing equations as defined in Equation (12) and expressed in polar coordinates, can consequently be simplified into the following system of **ordinary differential equations (ODEs)**:

$$\frac{v_\varphi^2}{r} - \frac{1}{\rho} \frac{dp}{dr} = 0 \quad \text{in } \Omega_{\text{inner}} , \quad (28a)$$

$$\frac{d^2 v_\varphi}{dr^2} + \frac{1}{r} \frac{dv_\varphi}{dr} - \frac{v_\varphi}{r^2} = 0 \quad \text{in } \Omega_{\text{inner}} . \quad (28b)$$

However, the assumptions defined in Equation (27) are not valid in Ω_{outer} ; there, Equation (12) must be solved. This insight motivates the idea of employing a **DD** approach, adapting the **XPINN** approach as outlined in Section 2.3. The decomposition is depicted in Figure 7a. We simultaneously train two **NNs**, solving only Equation (28) in Ω_{inner} to obtain solution variables $\mathbf{u}_{\text{inner}} = (v_{\text{inner},\varphi}, p_{\text{inner}})^T$ and solving Equation (12) in Ω_{outer} to obtain $\mathbf{u}_{\text{outer}} = (v_{\text{outer},r}, v_{\text{outer},\varphi}, p_{\text{outer}})^T$. The location of the interface between the two domains R_{inter} is a hyperparameter. For the model presented in this section we set $R_{\text{inter}} = 0.07$ m. We employ strong Dirichlet **BC** imposition on Γ_{stirrer} as defined in Section 4.6. The function used to normalize the inputs and rescale the outputs can be found in Appendix A.7. To ensure continuity of the solution variables and their derivatives, the following constraints are imposed on $\Gamma_{\text{inter}} = \partial\Omega_{\text{inner}}$:

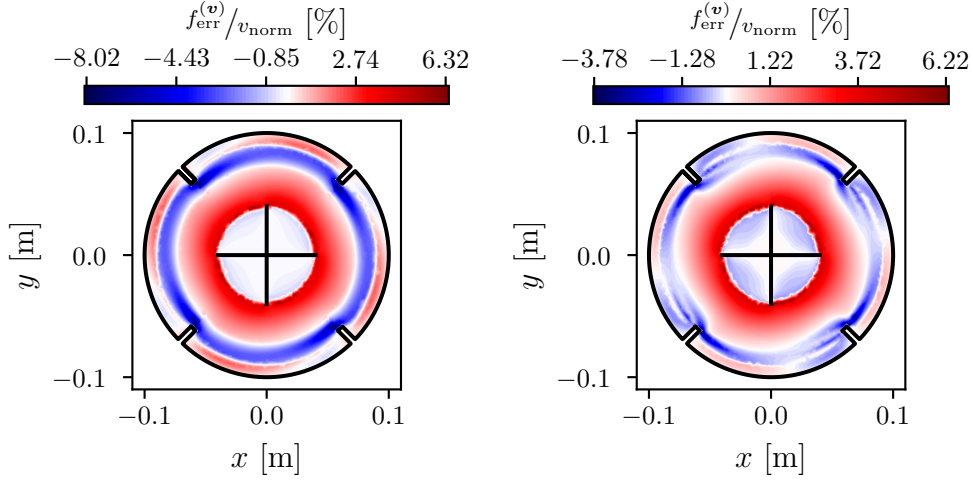
$$v_{\text{outer},r} = 0 \quad \text{on } \Gamma_{\text{inter}} , \quad (29a)$$

$$v_{\text{outer},\varphi} = v_{\text{inner},\varphi} \quad \text{on } \Gamma_{\text{inter}} , \quad (29b)$$

$$p_{\text{outer}} = p_{\text{inner}} \quad \text{on } \Gamma_{\text{inter}} , \quad (29c)$$

$$\frac{\partial v_{\text{outer},\varphi}}{\partial r} = \frac{dv_{\text{inner},\varphi}}{dr} \quad \text{on } \Gamma_{\text{inter}} . \quad (29d)$$

Since we solve a different set of equations in each subdomain, we omit the requirement of residual equality on the interface. As depicted in Figure 11a, this approach helps to reduce the average normalized error of the velocity predictions to approximately 1.5%. Moreover, we can observe that the error distribution is such that notable errors are confined to areas near the stirrer tips and the baffles. This error is associated with the inability of the PINN model to accurately replicate the kink in the velocity profile in radial direction at $\varphi = \pi/4$, as illustrated in Figure 13b. We tackle this source of error in the subsequent section.



(A) Spatial distribution of the normalized error in velocity magnitude predicted by the model using DD into two domains described in Section 4.7.

(B) Spatial distribution of the normalized error in velocity magnitude predicted by the model using DD with a split of Ω_{outer} presented in Section 4.8.

FIGURE 11. Spatial distribution of the normalized error in velocity magnitude predicted by the models using DD.

4.8. DD model with outer split. To capture the behavior illustrated in Figure 13b, we can enhance the DD approach by further splitting Ω_{outer} into two parts as follows:

$$\Omega_{\text{outer}}^{(1)} = \{(r, \varphi) \in \Omega_{\text{outer}} : r \leq R_{\text{baff}}\} , \quad (30a)$$

$$\text{and } \Omega_{\text{outer}}^{(2)} = \{(r, \varphi) \in \Omega_{\text{outer}} : r > R_{\text{baff}}\} . \quad (30b)$$

We split the circumferential velocity component by defining $v_{\text{outer},\varphi}^{(1)}$ and $v_{\text{outer},\varphi}^{(2)}$, respectively. We establish two distinct interfaces between the two regions: the continuity interface Γ_c and the derivative interface Γ_d . On Γ_c , only the continuity constraint

$$v_{\text{outer},\varphi}^{(1)} = v_{\text{outer},\varphi}^{(2)} \quad \text{on } \Gamma_c , \quad (31)$$

is considered. On the derivative interface Γ_d , the continuity of normal derivatives

$$\frac{\partial v_{\text{outer},\varphi}^{(1)}}{\partial r} = \frac{\partial v_{\text{outer},\varphi}^{(2)}}{\partial r} \quad \text{on } \Gamma_d, \quad (32)$$

is also imposed. The outer domain split is located at $R_{\text{outer}} = 0.0851$ m, right after the baffle. The derivative interface extends between $-0.3 \leq \varphi \leq 0.3$. As illustrated in Figure 7b, the derivative interface does not extend all the way to the baffles, thereby allowing for the accurate reproduction of the kink. Given that we define the circumferential velocity as the additional output $v_{\text{outer},\varphi}^{(2)}$ in $\Omega_{\text{outer}}^{(2)}$, the no-slip BC is expressed as

$$v_{\text{outer},\varphi}^{(2)} = 0 \quad \text{on } \Gamma_{\text{wall}}. \quad (33)$$

For the wall segment at the baffle, as illustrated in Figure 12, the no-slip BC applies to $v_{\text{outer},\varphi}^{(1)}$, making

$$v_{\text{outer},\varphi}^{(1)} = 0 \quad \text{on } \Gamma_{\text{baffle}}. \quad (34)$$

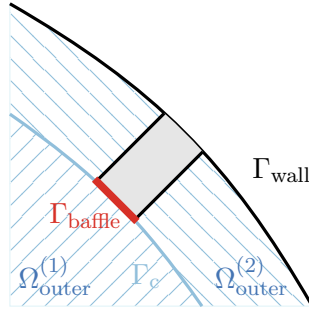


FIGURE 12. Close up of the upper right baffle for the DD models. The segment of the boundary highlighted in red, Γ_{baffle} , uniquely belongs to $\Omega_{\text{outer}}^{(1)}$, i.e., we need to prescribe a BC for $v_{\text{outer},\varphi}^{(1)}$, while the rest of the wall belongs to $\Omega_{\text{outer}}^{(2)}$ and we prescribe $v_{\text{outer},\varphi}^{(2)}$.

Splitting the outer domain into two regions not only reduces the mean normalized error of the velocity predicted by the PINN, but it also enhances the quality of the predicted velocity field. This improvement is illustrated in figure Figure 11b, where there are no prominent areas with concentrated higher error levels. Moreover, Figure 13 demonstrates that this model successfully replicates the velocity profile along the radius both for $\varphi = 0$ (Figure 13a) and $\varphi = \pi/4$ (Figure 13b).

4.9. Robustness study. Given that the training of a PINN involves an optimization process with a highly complex (and non-convex) objective function landscape, and stagnation in saddle points is a common challenge in high-dimensional optimization problems [8], we had to make sure our models are robust and reproducible with the specified hyperparameter settings. To address this, we conducted a robustness study by training the same model 10 times with different random initializations of the NNs' weights. As the model presented in Section 4.7 is the one chosen for subsequent parameterization, it is also employed to demonstrate the robustness study. We utilize the normalized velocity error defined in Equation (18) along the

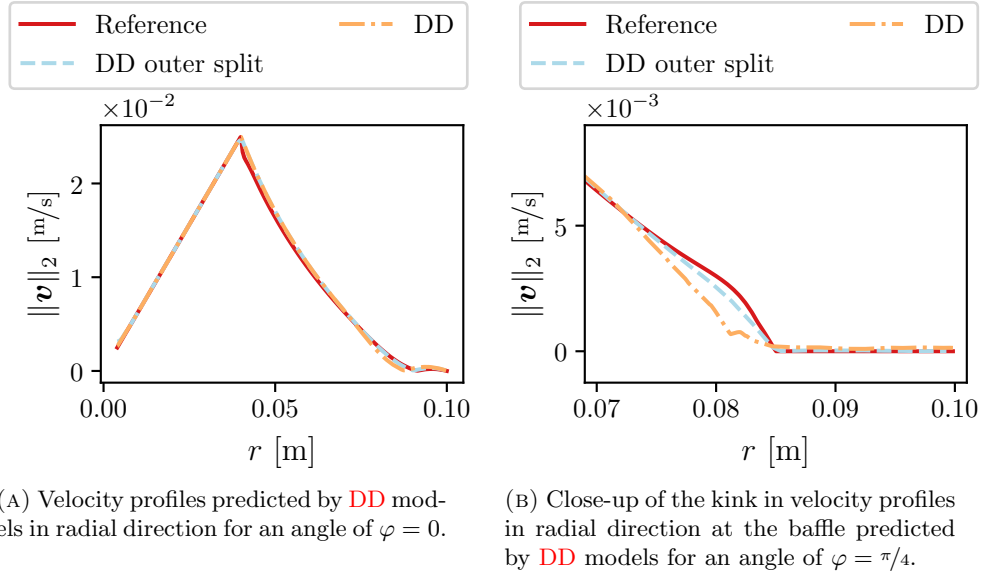


FIGURE 13. Profiles of velocity magnitude in radial direction r predicted by the DD models.

radius of the impeller for $\varphi = 0$ to showcase the model's robustness in Figure 14. The mean $\delta_{\ell^1}^{(v)}$ error across ten model runs is 1.43%, with a standard deviation $\sigma < 0.09\%$. Therefore, we can conclude that our proposed model reliably produces highly accurate predictions and is thus well-suited for further investigations.

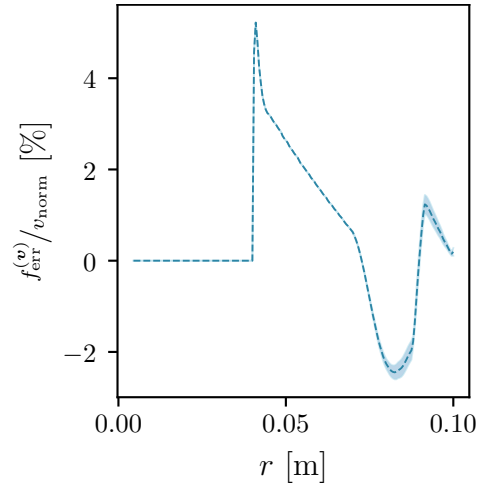


FIGURE 14. Mean value and standard deviation of the normalized error in velocity magnitude obtained from the repeated model training, measured in radial direction along an angle of $\varphi = 0$. The errors obtained from the different runs only differ by a very small amount in the outer region close to the wall.

4.10. **Model Configuration.** In our work, we used the **PINN** implementation provided by the `deepxde` python package [26] with Tensorflow [1] as backend. All models were trained on 50,000 domain points using minibatch sampling. The optimal size of the **NN** was determined through hyperparameter optimization using the `optuna` library [3]. The **NNs** employed in Sections 4.1 to 4.6 were 2 layers deep and 100 neurons wide. The parallel **NNs** employed in Sections 4.7 and 4.8 were 25 and 100 neurons wide, respectively, and 2 layers deep. We utilized the hyperbolic tangent activation function and applied ℓ^1 and ℓ^2 regularization. The loss function was logarithmically transformed, and the L-BFGS-B optimizer [4, 48] from the `scipy` python package [42] was employed to perform the minimization. The remaining hyperparameter settings for each model are detailed in Appendix A.

4.11. **Summary.** After presenting the different models, this section aims to equip the reader with the necessary information on which model to choose for their application. The errors and training times for each individual model are reported in Table 2. All models were trained on the GPUs of the high-performance computer Lichtenberg at the NHR Centers NHR4CES at TU Darmstadt. The reported computing times have been measured there. Note, that the training times generally depend on the available hardware and can differ across different machines. Consequently, they are to be understood more as a general guideline of how expensive the training of a certain model is in comparison to another.

TABLE 2. Model errors and training times for the **PINN** models discussed in Section 4.

Model	ℓ^1 errors [%]		ℓ^2 errors [%]		Time [min]
	$\delta_{\ell^1}^{(v)}$	$\delta_{\ell^1}^{(p)}$	$\delta_{\ell^2}^{(v)}$	$\delta_{\ell^2}^{(p)}$	
Baseline (Section 4.1)	10.74	9.48	16.41	14.62	8.70
Baseline Data (Section 4.2)	2.27	1.04	2.93	1.24	10.40
Baseline Scaled (Section 4.3)	3.88	2.49	6.47	4.63	8.62
Baseline Polar (Section 4.4)	3.66	1.14	4.89	1.64	5.80
Strong BC (Section 4.5)	5.11	2.26	7.44	2.68	61.93
Hybrid BC (Section 4.6)	3.22	1.20	4.31	1.43	65.08
DD (Section 4.7)	1.45	0.63	1.93	0.97	51.05
DD with outer split (Section 4.8)	0.97	0.74	1.41	1.28	71.10

Table 2 indicates that the model employing **DD** with an additional split of the outer domain presented in Section 4.8 achieves the most accurate predictions for

velocity, with $\delta_{\ell^1}^{(v)} < 1\%$. As evident from the error distribution in Figure 11b and the velocity profiles in Figure 13, this model also performs the best qualitatively in capturing the subtle behavior of the flow. However, the model presented in Section 4.7 performs slightly better in terms of capturing the pressure. Since it is overall less complex and more straightforward than the model defined in Section 4.8, we chose this model for further work, in particular parameterization by the stirring rate in Section 5. It is apparent from the table that strong BC imposition comes at a significant computational cost, increasing the training time by a factor of ~ 8 . However, enforcing Dirichlet BCs in a strong manner also reduces the number of loss components and thereby the number of hyperparameters that need to be selected. Thus, the time saved in selecting the optimal loss scaling factors should also be considered when comparing the models' training times. Moreover, employing polar coordinates and leveraging the symmetry of the model by only training on Ω_{sym} , as described in Section 4.4, results in the shortest training time.

5. Parameterized case. After identifying the model from Section 4.7 as the best performing model, we parameterize it based on the rotational velocity of the impeller ω to enable predictions for $\text{Re} \in [1000, 10,000]$. We achieve this by extending the polar domain Ω_{polar} by the parameter space $\Lambda = [\omega_{\min}, \omega_{\max}]$, where ω_{\min} and ω_{\max} for the respective Re are calculated using Equation (16). In terms of the notation presented in Section 2, $\mathcal{X} = \Omega_{\text{polar}} \times \Lambda$. During the NN training, we do not only randomly generate points in Ω_{polar} , but additionally draw points from a uniform distribution over Λ . This section introduces the configuration and results of the parameterized model and subsequently explores the implementation of strong constraints for the domain interface as a means to reduce the number of the model's hyperparameters.

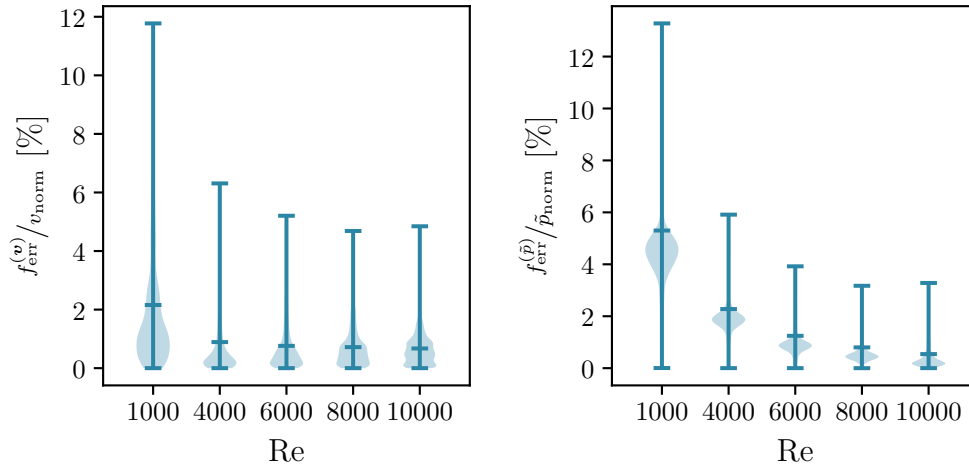
5.1. DD model. In this model, the configuration outlined in Section 4.7 was utilized, including output scaling and normalization of $\mathbf{x}_{\text{polar}}$. The normalized parametric input, $\tilde{\omega} \in [-1, 1]$, was obtained as follows:

$$\tilde{\omega} = \frac{\omega - \omega_{\text{avg}}}{\omega_{\max} - \omega_{\text{avg}}}, \quad (35)$$

where

$$\omega_{\text{avg}} = \frac{\omega_{\min} + \omega_{\max}}{2}. \quad (36)$$

The position of the domain interface was chosen as $R_{\text{inter}} = 0.075$ m. The training of this model took 148.7 min. The distributions of normalized velocity and pressure errors for selected values of Re are depicted in Figure 15. It is evident that the model is capable of providing very accurate predictions for velocity and reasonably accurate predictions for pressure within the trained parametric range. Furthermore, parameterizing the model results in an improved mean velocity error for $\text{Re} = 4000$ compared to the non-parameterized model in Section 4.7, achieving $\delta_{\ell^1}^{(v)} = 0.9\%$. The relatively larger errors observed for $\text{Re} = 1000$, primarily concentrated in the inner domain near the stirrer tip as illustrated in Figure 16a, can be explained by examining the profile of the boundary function \mathbf{v}_{BC} , used to enforce strong boundary constraints on Γ_{stirrer} in Figure 16b (the definition of \mathbf{v}_{BC} can be found in Appendix C). While this function offers a good approximation of the kink in velocity at the stirrer tip for $\text{Re} = 4000$, the sharper kink at a lower Re results in the boundary function being a less accurate representation of the velocity field.



(A) Distribution of normalized errors in velocity magnitude for selected values of Re.

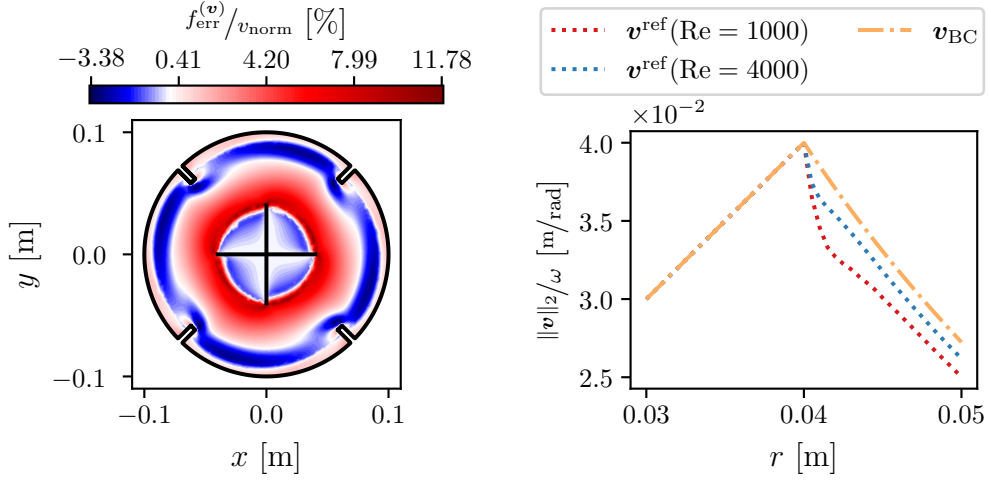
(B) Distribution of normalized errors in pressure for selected values of Re.

FIGURE 15. Distributions of velocity and pressure errors for selected values of Re of the model parameterized by ω using soft continuity constraints on the subdomain interface. The ends of the bars indicate minimum and maximum errors, while the additional bar in between represents the mean value, which corresponds to $\delta_{\ell_1}^{(q)}$ in Equation (19). The overall performance of the model improves with increasing Re.

Consequently, the NN has to make more corrections to this approximation, leading to larger errors. As depicted in Figure 16a, another region where higher errors are concentrated is in the vicinity of the baffles and the wall. This can be attributed to the fact that for low Re, the velocity values in this region are very small, making the network more prone to learning the trivial solution, i.e., $\mathbf{v} = \mathbf{0}$. The combination of this fact and the previously mentioned characteristics of the velocity profile provides an explanation for why the model’s overall performance improves at higher Re.

By contrast, pressure predictions are only reasonably accurate. While it might be conceivable to enhance the model’s ability to predict pressure through a different selection of loss component scaling factors, exploring all possible combinations becomes impractical due to the extensive parameter space. In the following section, we attempt to address this challenge.

5.2. DD model with domain overlap. As previously demonstrated in Section 4, the decision regarding the scaling of individual loss components can profoundly affect the model’s prediction capabilities. One of the primary challenges of the model employing DD is that, due to the different sets of equations in each subdomain and the additional coupling constraints on Γ_{inter} , its objective function comprises 14 contributions that require scaling. In an effort to reduce the number of loss component scaling factors that need to be chosen, we can employ Equation (10) to enforce strong constraints for the interface. Following an approach similar to the one outlined in [29], this is achieved by establishing a slight overlap between the two subdomains, as illustrated in Figure 17. Within the overlap region, we augment the



(A) Spatial distribution of the error in velocity magnitude. Comparatively large errors are localized in the inner domain right at the stirrer tip and in the outer domain near the baffles and reactor walls.

(B) Velocity profiles along the radius at $\varphi = 0$ normalized through the division by ω . The reference profile for $\text{Re} = 1000$ exhibits a sharper kink than the one approximated by the boundary function v_{BC} .

FIGURE 16. Sources of error in the velocity predictions made by the parameterized model for $\text{Re} = 1000$. Spatial distribution of velocity error within the domain (A) and comparison of the velocity profile approximated by the boundary function v_{BC} with profiles of the reference solution for $\text{Re} = 1000$ and $\text{Re} = 4000$ (B).

output of our **PINN** model in the post-processing step by two auxiliary variables, $v_{\varphi, \text{overlap}}$ and p_{overlap} , which are defined as follows:

$$v_{\text{overlap}, \varphi}(\mathbf{x}) = g_{\text{overlap}}(\mathbf{x})v_{\text{inner}, \varphi}(\mathbf{x}) + (1 - g_{\text{overlap}}(\mathbf{x}))v_{\text{outer}, \varphi}(\mathbf{x}), \quad (37a)$$

$$p_{\text{overlap}}(\mathbf{x}) = g_{\text{overlap}}(\mathbf{x})p_{\text{inner}}(\mathbf{x}) + (1 - g_{\text{overlap}}(\mathbf{x}))p_{\text{outer}}(\mathbf{x}). \quad (37b)$$

Here g_{overlap} is a distance function defined as

$$\begin{cases} g_{\text{overlap}}(\mathbf{x}) = 0 & \text{on } \Gamma_{\text{out}} \\ g_{\text{overlap}}(\mathbf{x}) = 1 & \text{on } \Gamma_{\text{in}} \end{cases}, \quad (38)$$

which we again determine following the approach proposed in [36]. By ensuring the continuity of v_{φ} and p in this manner, we can replace all of the constraints defined in Equation (29) except for Equation (29a), which we still impose weakly, since $v_{\text{inner}, r} \equiv 0$. Additionally, as shown in Figure 18, the accuracy of the model's velocity predictions is comparable to the model defined in Section 5.1. Moreover, the present model captures the pressure more accurately. However, it is crucial to note that the increase in training time for this model ranges between 25 % and 30 % when compared to the model with weak interface constraints. Nevertheless, this extra time is offset by the spared efforts in selecting the proper scaling factors for the loss components corresponding to continuity constraints.

5.3. Summary. The model detailed in Section 5.1 employing weak coupling constraints on Γ_{inter} achieves a mean velocity error ranging from 0.6 % to 2 % across the

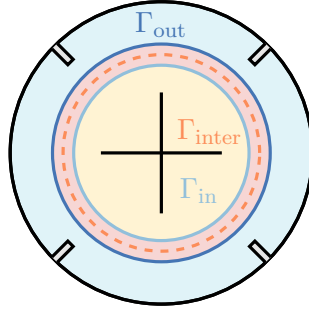
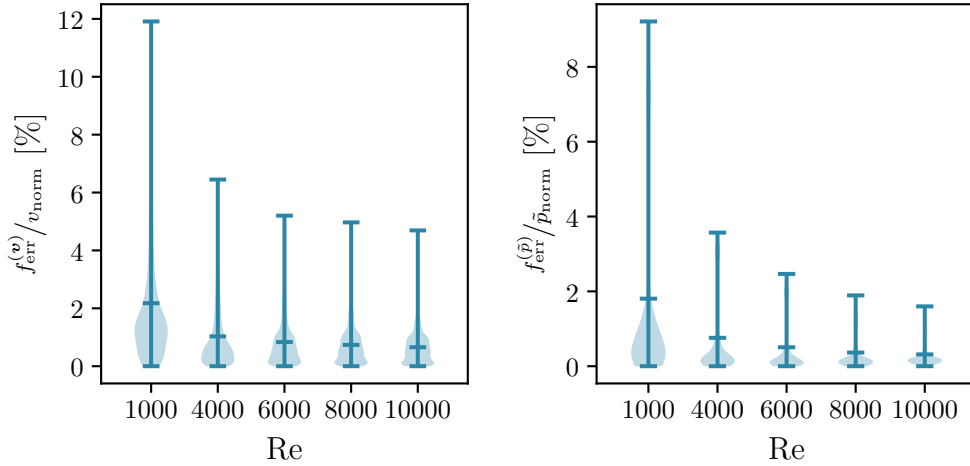


FIGURE 17. Schematic illustrating the domain overlap defined in Section 5.2 and the bounds Γ_{in} and Γ_{out} within which the distance function $g_{overlap}$ is defined.



(A) Error distribution of velocity magnitude predictions for selected values of Re .

(B) Error distribution of pressure predictions for selected values of Re .

FIGURE 18. Velocity and pressure error distributions for selected values of Re of the model parameterized by ω with overlapping domains.

range $Re \in [1000, 10,000]$. However, its performance in pressure prediction, with $\delta_{\ell_1}^{(p)}$ as high as 6% is less satisfactory. By enforcing continuity across the domain interface in a strong manner in Section 5.2, we improve the pressure prediction capabilities, achieving $\delta_{\ell_1}^{(p)}$ between 0.3% to 1.8%, while maintaining the same prediction capabilities for velocity. This improvement is attributed to the elimination of the need to optimize the scaling of loss components representing the velocity and pressure coupling.

6. Conclusions. In this paper, we explore various strategies to enhance the performance of PINN models for simulating the flow in a 2D STR. In its most basic configuration, the PINN model produces unsatisfactory results for this application

case. While integrating a data loss into the training significantly improves prediction capabilities, acquiring such extensive data is often impractical for our application, particularly when considering parameterized models. Therefore, we address the limitations of the baseline **PINN** model without relying on labeled training data. Instead, we incorporate additional insights into the physics of the problem derived from the reference solution. We introduce and compare a series of models with varying levels of complexity and accuracy, which we believe can similarly be adapted to different applications. To prove the reproducibility of our results, we examine the robustness of our models and provide detailed reports of the settings of our configurations.

We show that imposing Dirichlet **BCs** in a strong manner helps to capture kinks in the solution field. Additionally, we observe that the choice of the **BC** function \mathbf{h} is not arbitrary; the better it represents the physics, the better the prediction capabilities of the model are. Employing **DD** allows us to harness the distinct flow character in different regions of the domain, resulting in both qualitative and quantitative improvements in the model’s predictions. Moreover, we showcase that the **XPINN** and **DPINN** approaches can be adapted for cases where different sets of equations are solved in each subdomain, which — to the best of our knowledge — has not been demonstrated in the literature before.

Leveraging the symmetry of the problem and employing polar coordinates yields the shortest training time. Although this model sacrifices some accuracy, it can prove valuable in applications where speed is the top priority. **DD** can be used to train models of the highest accuracy which can serve as basis for detailed analysis of the **STR**. After showcasing that this model reliably makes highly accurate predictions, we have chosen it for subsequent parameterization by the stirring rate, due to its performance and relative simplicity.

Through parameterization, we obtain a model achieving a mean velocity error below 2% across the range $\text{Re} \in [1000, 10,000]$, but falling short in pressure prediction. We address this limitation by imposing the continuity across the domain interface in a strong manner. By doing so, we reduce the complexity of hyperparameter selection, as we no longer need to optimize the scaling of loss components that account for the coupling of velocity and pressure between the different domains.

Although the training times of the nonparameterized models cannot compete with classical numerical methods, our objective is not to compete in this aspect. Instead, these models serve as preliminary steps for subsequent parameterization. As we demonstrate the interpolation capability of parameterized models within the parameter space, the time required to train one model should be compared with the time needed to conduct numerous numerical simulations. Given that selecting hyperparameters, particularly scaling the loss function components, remains challenging and time-consuming, we mitigate this by enforcing interface continuity constraints strongly, thus reducing the number of these components.

Our ultimate goal is to apply the methodologies outlined in this work to higher-dimensional models, encompassing both physical and parameter spaces. Moreover, these approaches can be adapted and applied to other complex flow problems beyond the scope of this paper.

Use of AI tools declaration. The authors declare they have used Artificial Intelligence (AI) tools in the creation of this article: In some paragraphs throughout the

article, AI tools have been used to rephrase and improve sentences grammatically and language-wise. We emphasize that no content has been generated by AI tools.

Acknowledgments. This work was performed as part of the Helmholtz School for Data Science in Life, Earth and Energy (HDS-LEE) and received funding from the Helmholtz Association of German Research Centres. This work was supported by the Deutsche Forschungsgemeinschaft (DFG, German Research Foundation) – 333849990/GRK2379 (IRTG Hierarchical and Hybrid Approaches in Modern Inverse Problems). The authors gratefully acknowledge the computing time provided to them on the high-performance computer Lichtenberg at the NHR Centers NHR4CES at TU Darmstadt. This is funded by the Federal Ministry of Education and Research, and the state governments participating on the basis of the resolutions of the GWK for national high performance computing at universities (www.nhr-verein.de/unsere-partner). The authors gratefully acknowledge the computing time granted by the JARA Vergabegremium and provided on the JARA Partition part of the supercomputer CLAIX at RWTH Aachen University.

Furthermore the authors want to acknowledge the work of Henri Lubjuhn who developed larger parts of the authors' software framework for conducting the **PINN** trainings during his seminar and master's theses.

Appendix A. Supplementary information and hyperparameters for the models presented in Section 4.

A.1. **Baseline model.** The hyperparameters used for the training of the model presented in Section 4.1 are contained in Table 3. The boundary points were fixed throughout all epochs, whereas the domain points were resampled.

TABLE 3. Hyperparameters of the baseline model presented in Section 4.1.

	Hyperparameter	Value
Architecture	Number of layers	2
	Number of neurons per layer	100
	Activation function	tanh
Loss function	Regularization	$\ell^1 + \ell^2$
	Loss scaling	$\alpha_{\text{momentum},x} = 1$
		$\alpha_{\text{momentum},y} = 1$
		$\alpha_{\text{mass}} = 1$
		$\alpha_{\text{wall}} = 1$
$\alpha_{\text{impeller}} = 1$		
Optimization	Optimizer	L-BFGS-B
	Epochs	25,000
Sampling	Number of domain points	2048
	\leftrightarrow Resampled every	1000 epochs
	Number of boundary points	1024 on Γ_{stirrer} 1024 on Γ_{wall}

A.2. **Baseline model with data.** The hyperparameters used for the training of the model presented in Section 4.2 are mostly identical with the ones reported in Table 3. The additional hyperparameters are listed in Table 4. The data points were not resampled between the different epochs.

TABLE 4. Additional hyperparameters of the baseline model with data presented in Section 4.2.

	Hyperparameter	Value
Loss function	Loss scaling	$\alpha_{\text{data}} = 1$
Sampling	Number of data points	2000

A.3. **Baseline model with loss scaling.** The hyperparameters used for the training of the model presented in Section 4.3 are identical with the ones from Table 3 except for the loss scaling factors. These have been reported in Table 5.

TABLE 5. Modifications of the hyperparameters of the baseline model with loss scaling presented in Section 4.3.

Hyperparameter		Value
Loss function	Loss scaling	$\alpha_{\text{momentum},x} = 5 \times 10^1$
		$\alpha_{\text{momentum},y} = 5 \times 10^1$
		$\alpha_{\text{mass}} = 5 \times 10^1$
		$\alpha_{\text{wall}} = 5$
		$\alpha_{\text{impeller}} = 1$

A.4. **Baseline model in polar coordinates.** The hyperparameters used for the training of the model presented in Section 4.4 are reported in Table 6. Values that are not reported there are identical with the values reported in Table 3.

TABLE 6. Modifications and additions of the hyperparameters of the baseline model in polar coordinates presented in Section 4.4.

Hyperparameter		Value
Loss function	Loss scaling	$\alpha_{\text{momentum},r} = 1 \times 10^6$
		$\alpha_{\text{momentum},\varphi} = 1 \times 10^6$
		$\alpha_{\text{mass}} = 1$
		$\alpha_{\text{wall},v_r} = 1 \times 10^1$
		$\alpha_{\text{wall},v_\varphi} = 1 \times 10^1$
		$\alpha_{\text{impeller},v_r} = 5$
		$\alpha_{\text{impeller},v_\varphi} = 5$
		$\alpha_{\text{symmetry},v_r} = 1 \times 10^2$
		$\alpha_{\text{symmetry},v_\varphi} = 1 \times 10^2$
	$\alpha_{\text{symmetry},p} = 1$	
Optimization	Epochs	12,500
Sampling	Number of domain points	4096
	\leftrightarrow Resampled every	1000 epochs
		512 on Γ_{stirrer}
	Number of boundary points	512 on Γ_{wall} 1024 on Γ_{sym}

A.5. **Strong BC model.** Table 7 lists the hyperparameters used for the model presented in Section 4.5. Due to the strong BC imposition, no scaling factors for the boundary losses are reported.

TABLE 7. Hyperparameters of the strong BC model presented in Section 4.5.

	Hyperparameter	Value
Architecture	Number of layers	2
	Number of neurons per layer	100
	Activation function	tanh
Loss function	Regularization	$\ell^1 + \ell^2$
	Loss scaling	$\alpha_{\text{momentum},x} = 1$
		$\alpha_{\text{momentum},y} = 1$
		$\alpha_{\text{mass}} = 1$
Optimization	Optimizer	L-BFGS-B
	Epochs	25,000
Sampling	Number of domain points	2048
	\hookrightarrow Resampled every	1000 epochs

A.6. **Hybrid BC model.** For the model with hybrid BCs from Section 4.6, all hyperparameters are identical with the ones reported in Table 7, just one additional scaling factor for the wall BC is needed. Additionally, points on Γ_{wall} need to be sampled. These changes are reported in Table 8.

TABLE 8. Hyperparameters of the hybrid BC model presented in Section 4.6.

	Hyperparameter	Value
Loss function	Loss scaling	$\alpha_{\text{wall}} = 1$
Sampling	Number of boundary points	1024 on Γ_{wall}

A.7. **DD model.** For the DD models, we require significantly more hyperparameters: On the one hand, we now have multiple networks with different architectures and on the other hand, the loss function consists of significantly more terms, consequently resulting in more scaling factors. The hyperparameters for the model presented in Section 4.7 are reported in Table 9.

TABLE 9. Hyperparameters of the DD model with two domains presented in Section 4.7.

	Hyperparameter	Value	
Architecture	Network for inner region		
	↔ Number of layers	2	
	↔ Number of neurons per layer	25	
	Network for outer region		
	↔ Number of layers	2	
	↔ Number of neurons per layer	100	
	Activation function	tanh	
Loss function	Regularization	$\ell^1 + \ell^2$	
	Loss scaling	$\alpha_{\text{momentum},r} = 1 \times 10^9$ (inner region)	
		$\alpha_{\text{momentum},\varphi} = 1 \times 10^8$ (inner region)	
		$\alpha_{\text{momentum},r} = 5 \times 10^{13}$ (outer region)	
		$\alpha_{\text{momentum},\varphi} = 5 \times 10^{14}$ (outer region)	
		$\alpha_{\text{mass}} = 5 \times 10^8$ (outer region)	
		$\alpha_{\text{coupling},v_r} = 1 \times 10^{12}$	
		$\alpha_{\text{coupling},v_\varphi} = 1 \times 10^{12}$	
		$\alpha_{\text{coupling},\partial_r v_\varphi} = 1 \times 10^7$	
		$\alpha_{\text{coupling},p} = 1 \times 10^6$	
		$\alpha_{\text{wall},v_r} = 1 \times 10^{10}$	
		$\alpha_{\text{wall},v_\varphi} = 1 \times 10^{13}$	
		$\alpha_{\text{symmetry},v_r} = 1 \times 10^9$	
		$\alpha_{\text{symmetry},v_\varphi} = 1 \times 10^9$	
$\alpha_{\text{symmetry},p} = 1 \times 10^5$			
Optimization	Optimizer	L-BFGS-B	
	Epochs	12,500	
Sampling	Number of domain points	4096	
	↔ Resampled every	1000 epochs	
	↔ Position of R_{inter}	0.07	
	↔ Ratio of points in $\Omega_{\text{inner}}/\Omega_{\text{outer}}$	0.2	
	Number of boundary points		256 on Γ_{wall}
			512 on Γ_{sym}
		256 on Γ_{inter}	

Since we are solving the set of ODEs defined in Equation (28) in Ω_{inner} , which is independent of φ , and we exploit symmetry of Ω_{outer} in the same manner as discussed in Section 4.4, the input pre-processing function from Equation (9) is defined as follows:

$$\tilde{\mathbf{x}} = \begin{pmatrix} r_{\text{inner}} \\ r_{\text{outer}} \\ \varphi_{\text{outer}} \end{pmatrix} = f^{\text{pre}}(\mathbf{x}_{\text{polar}}) = \begin{pmatrix} (r - R_{\text{stirrer}})/(R_{\text{inter}} - R_{\text{stirrer}}) \\ (r + 0.5R_{\text{reactor}} - 1.5R_{\text{inter}})/0.5(R_{\text{reactor}} - R_{\text{inter}}) \\ 4\varphi/\pi \end{pmatrix}. \quad (39)$$

The non-dimensional outputs of the NN in Ω_{inner} are scaled as:

$$\mathbf{u}_{\text{inner}} = \mathbf{f}_{\text{post}}(\tilde{\mathbf{u}}_{\text{inner}}) = \begin{pmatrix} \|v_{\text{tip}}\| \tilde{v}_{\text{inner},\varphi} \\ \rho v_{\text{tip}}^2 \tilde{p}_{\text{inner}} \end{pmatrix}. \quad (40)$$

Consequently, the Dirichlet BC at Γ_{stirrer} is imposed in a strong manner by applying Equation (10) to $v_{\text{inner},\varphi}$. The outputs in Ω_{outer} are scaled as follows:

$$\mathbf{u}_{\text{outer}} = \mathbf{f}_{\text{post}}(\tilde{\mathbf{u}}_{\text{outer}}) = \begin{pmatrix} v_{\text{norm},r} \tilde{v}_{\text{outer},r} \\ |v_{\text{norm},\varphi}| \tilde{v}_{\text{outer},\varphi} \\ \rho \|\mathbf{v}_{\text{norm}}\|_2^2 \tilde{p}_{\text{outer}} \end{pmatrix}, \quad (41)$$

where $v_{\text{norm},r} = v_{r,\text{max}}^{\text{ref}}$,

$$v_{\text{norm},\varphi} = v_{\text{tip}} \frac{R_{\text{stirrer}}(R_{\text{inter}}^2 - R_{\star}^2)}{R_{\text{inter}}(R_{\text{stirrer}}^2 - R_{\star}^2)}, \quad (42)$$

and $\mathbf{v}_{\text{norm}} = (v_{\text{norm},r}, v_{\text{norm},\varphi})^T$. Here, $R_{\star} = 0.0875$ m is chosen as the approximate point where the reference velocity profile depicted in Figure 19 hits zero. As the equations solved in Ω_{inner} do not depend on φ , we only sample points with $\varphi = 0$ in this domain.

A.8. **DD model with outer split.** For the model with the additional split in the outer domain as introduced in Section 4.8, the loss function is even further augmented by additional terms. The respective hyperparameters are reported in Table 10. All values that are not reported coincide with what has been already listed in Table 9.

TABLE 10. Hyperparameters of the DD model with outer domain split presented in Section 4.8.

Hyperparameter	Value
	$\alpha_{\text{momentum},r} = 1 \times 10^{11}$ (inner region)
	$\alpha_{\text{momentum},\varphi} = 1 \times 10^8$ (inner region)
	$\alpha_{\text{momentum},r} = 4 \times 10^{16}$ (outer region)
	$\alpha_{\text{momentum},\varphi} = 4 \times 10^{16}$ (outer region)
	$\alpha_{\text{mass}} = 4 \times 10^{10}$ (outer region)
	$\alpha_{\text{coupling},v_r} = 1$
	$\alpha_{\text{coupling},v_\varphi} = 1 \times 10^{14}$
	$\alpha_{\text{coupling},\partial_r v_\varphi} = 1 \times 10^8$
Loss function	$\alpha_{\text{coupling},p} = 1 \times 10^6$
Loss scaling	$\alpha_{\text{wall},v_r} = 1 \times 10^{14}$
	$\alpha_{\text{wall},v_\varphi} = 1 \times 10^{15}$
	$\alpha_{\text{symmetry},v_r} = 1$
	$\alpha_{\text{symmetry},v_\varphi} = 1 \times 10^{10}$
	$\alpha_{\text{symmetry},p} = 1 \times 10^5$
	$\alpha_{\text{baffle}} = 1 \times 10^{14}$
	$\alpha_c = 1 \times 10^{13}$
	$\alpha_d = 1 \times 10^8$
	Number of domain points 4096
	\hookrightarrow Resampled every 1000 epochs
	\hookrightarrow Position of R_{inter} 0.08
	\hookrightarrow Ratio of points in $\Omega_{\text{inner}}/\Omega_{\text{outer}}$ 0.2
Sampling	528 on Γ_{wall}
	512 on Γ_{sym}
	Number of boundary points 256 on Γ_{inter}
	256 on Γ_c
	512 on Γ_{baffle}

For this model, the input and output scaling described in Appendix A.7 are applied. The additional output $v_{\text{outer},\varphi}^{(2)}$ is scaled by a factor of 1×10^{-3} .

Appendix B. Supplementary information and hyperparameters for the models presented Section 5. For both parameterized models outlined in Sections 5.1 and 5.2 utilizing DD, we employ the same NN architecture as described in the nonparameterized model in Section 4.7. The differences from the nonparameterized model are evident in the selection of loss scaling factors. Additionally, it is crucial to highlight that for both parameterized models, the sampled domain points in Ω_{inner} are not restricted to $\varphi = 0$. Instead, sampling is performed for all values of $\varphi \in [0, 2\pi)$ and $\omega \in [\omega_{\text{min}}, \omega_{\text{max}}]$.

B.1. **DD model.** The hyperparameters for the parameterized **DD** model from Section 5.1 are reported in Table 11.

TABLE 11. Hyperparameters of the parameterized **DD** model with two domains presented in Section 5.1.

	Hyperparameter	Value	
Architecture	Network for inner region		
	↔ Number of layers	2	
	↔ Number of neurons per layer	25	
	Network for outer region		
	↔ Number of layers	2	
	↔ Number of neurons per layer	100	
	Activation function	tanh	
Loss function	Regularization	$\ell^1 + \ell^2$	
	Loss scaling	$\alpha_{\text{momentum},r} = 1 \times 10^3$ (inner region)	
		$\alpha_{\text{momentum},\varphi} = 1$ (inner region)	
		$\alpha_{\text{momentum},r} = 1 \times 10^7$ (outer region)	
		$\alpha_{\text{momentum},\varphi} = 1 \times 10^8$ (outer region)	
		$\alpha_{\text{mass}} = 1 \times 10^3$ (outer region)	
		$\alpha_{\text{coupling},v_r} = 1 \times 10^7$	
		$\alpha_{\text{coupling},v_\varphi} = 1 \times 10^9$	
		$\alpha_{\text{coupling},\partial_r v_\varphi} = 1 \times 10^8$	
		$\alpha_{\text{coupling},p} = 1 \times 10^3$	
		$\alpha_{\text{wall},v_r} = 1 \times 10^2$	
		$\alpha_{\text{wall},v_\varphi} = 1 \times 10^4$	
		$\alpha_{\text{symmetry},v_r} = 1$	
$\alpha_{\text{symmetry},v_\varphi} = 1$			
$\alpha_{\text{symmetry},p} = 1 \times 10^2$			
Optimization	Optimizer	L-BFGS-B	
	Epochs	30,000	
Sampling	Number of domain points	4096	
	↔ Resampled every	1000 epochs	
	↔ Position of R_{inter}	0.075	
	↔ Ratio of points in $\Omega_{\text{inner}}/\Omega_{\text{outer}}$	2.3	
	Number of boundary points		256 on Γ_{wall}
			512 on Γ_{sym}
		256 on Γ_{inter}	

The pre- and postprocessing functions defined in Equations (39) to (41) are employed. As the scaling for $v_{\text{outer},r}$ in the form of $v_{\text{norm},r}$ now varies with ω , we adapt the scaling accordingly as:

$$v_{\text{norm},r}(\omega) = 4 \times 10^{-4} \omega^2 + 1.2 \times 10^{-3} \omega. \quad (43)$$

B.2. **DD model with domain overlap.** The model with overlapping domains defined in Section 5.2 employs the same set of hyperparameters as the model with soft coupling constraints in Section 5.1, with the exception of the loss scaling factors.

The input and output scaling procedures are also identical. Furthermore, strong coupling constraints are enforced by applying Equation (37) to the scaled outputs and additional points are sampled in the domain overlap. The modifications of the hyperparameters with respect to the ones already reported in Table 11 are listed in Table 12.

TABLE 12. Hyperparameters of the parameterized DD model with domain overlap presented in Section 5.2.

Hyperparameter		Value
Loss function	Loss scaling	$\alpha_{\text{momentum},r} = 1 \times 10^5$ (inner region)
		$\alpha_{\text{momentum},\varphi} = 1$ (inner region)
		$\alpha_{\text{momentum},r} = 1 \times 10^9$ (outer region)
		$\alpha_{\text{momentum},\varphi} = 1 \times 10^9$ (outer region)
		$\alpha_{\text{mass}} = 1 \times 10^4$ (outer region)
		$\alpha_{\text{coupling},v_r} = 1 \times 10^7$
		$\alpha_{\text{wall},v_r} = 1 \times 10^4$
		$\alpha_{\text{wall},v_\varphi} = 1 \times 10^4$
		$\alpha_{\text{symmetry},v_r} = 1$
		$\alpha_{\text{symmetry},v_\varphi} = 1$
		$\alpha_{\text{symmetry},p} = 1 \times 10^2$
Sampling	Number of domain points	4096
	\leftrightarrow Resampled every	1000 epochs
	\leftrightarrow Ratio of points in $\Omega_{\text{inner}}/\Omega_{\text{outer}}$	0.125
	Number of domain overlap points	1536
	\leftrightarrow Width of overlap	0.01

Appendix C. Boundary function approximating the flow field. In the following we derive the functions \tilde{v}_{BC} and v_{BC} that are used to strongly impose the BCs of our model problem for the models presented in Sections 4.5 to 4.8. For more convenient notation, the functions are derived in polar coordinates.

From Equation (15) it follows that

$$v_r = 0 \quad \text{on} \quad \Gamma_{\text{stirrer}} \cup \Gamma_{\text{wall}}. \quad (44)$$

We can therefore set $\tilde{v}_{\text{BC},r} = v_{\text{BC},r} = 0$ in the whole domain to satisfy all Dirichlet BCs.

As pointed out in Section 4.5, our findings indicate that the choice of the boundary functions greatly influences the model predictions. Consequently, we aim to define $\tilde{v}_{\text{BC},\varphi}$ such that it approximates the reference velocity profile illustrated in Figure 19. We can observe that the behavior of v_φ^{ref} distinctly differs between the impeller region $r \leq R_{\text{stirrer}}$ and the outer region $R_{\text{stirrer}} < r < R_{\text{reactor}}$. This motivates a piece-wise definition of $\tilde{v}_{\text{BC},\varphi}$, which increases linearly in the stirrer region and then decays with unknown slope in the outer region. Since the increase in the inner region is given by the BC Equation (15b), we have

$$\tilde{v}_{\text{BC},\varphi} = \begin{cases} \omega r & r \leq R_{\text{stirrer}} \\ \tilde{v}_{\text{BC},\text{outer},\varphi}(r) & R_{\text{stirrer}} < r \end{cases}, \quad (45)$$

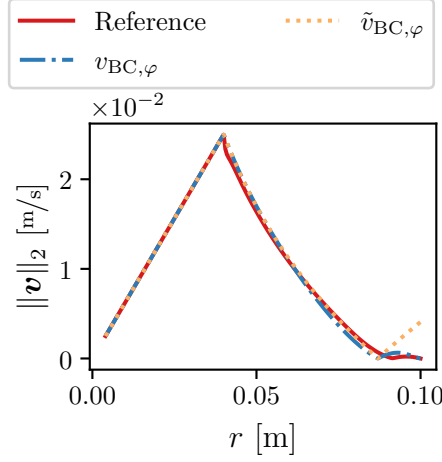


FIGURE 19. Reference velocity profile along the radius at $\varphi = 0$ for $\text{Re} = 4000$ and the function \mathbf{v}_{BC} constructed to approximate it.

where $\tilde{v}_{\text{BC,outer},\varphi}$ models the decay of the reference solution observed in Figure 19 for $r > R_{\text{stirrer}}$. In order to obtain a continuous profile, we know that $\tilde{v}_{\text{BC,outer},\varphi}(R_{\text{stirrer}}) = \omega r$. Moreover, we observe that the profile flattens out and approaches 0 at some $R_\star \gg R_{\text{stirrer}}$, i.e., $\tilde{v}_{\text{BC,outer},\varphi}(R_\star) = 0$. As detailed in Section 4.7, the governing equations can be approximated by an ODE system under some simplifying assumptions. Equipped with the conditions just mentioned, i.e.,

$$\tilde{v}_{\text{BC,outer},\varphi}(r) = \omega r \quad \text{at } r = R_{\text{stirrer}} , \quad (46a)$$

$$\tilde{v}_{\text{BC,outer},\varphi}(r) = 0 \quad \text{at } r = R_\star , \quad (46b)$$

Equation (28b) can be solved analytically and we choose its solution as $\tilde{v}_{\text{BC,outer},\varphi}$, i.e., we have

$$\tilde{v}_{\text{BC,outer},\varphi}(r) = \omega R_{\text{stirrer}} \frac{R_{\text{stirrer}}(r^2 - R_\star^2)}{r(R_{\text{stirrer}}^2 - R_\star^2)} , \quad (47)$$

where R_\star is a tuning parameter to adjust the slope of the velocity profile. For our application, we chose a value of $R_\star = 0.0875$ m which is approximately the location where the reference velocity profile depicted in Figure 19 flattens out.

We should note, that $\tilde{v}_{\text{BC},\varphi}$ defined in Equation (45) does not fulfill the BC on the wall as illustrated in Figure 19. While this is sufficient for the models with hybrid boundary constraints where we only strongly enforce the BC on the impeller, it is not suitable for the model presented in Section 4.5. Therefore, we propose an additional weighting inspired by the construction of the boundary function $\mathbf{g}(\mathbf{x})$ in [36], which reads

$$s(r) = (1 - [1 - l(r)]^\mu) , \quad (48)$$

where $l(r)$ is a spline constructed following the approach outlined in [36] to fulfill the condition

$$\begin{cases} l(r) = 0 & \text{on } \Gamma_{\text{wall}} \\ l(r) > 0 & \text{in } \Omega_{\text{polar}} \setminus \Gamma_{\text{wall}} \end{cases} , \quad (49)$$

and the hyperparameter $\mu = 8$ is set for this application. With that, a $v_{\text{BC},\varphi}$ which also fulfills the wall BC is obtained as

$$v_{\text{BC},\varphi}(r) = s(r)\tilde{v}_{\text{BC},\varphi}(r). \quad (50)$$

Remark: As pointed out in the beginning of this section, we report the boundary functions in polar coordinates as it simplifies their derivation. In order to employ them for the models presented in Sections 4.5 and 4.6 which use Cartesian coordinates as input, the functions have to be composed with a mapping from Cartesian to polar coordinates accordingly.

REFERENCES

- [1] M. Abadi, P. Barham, J. Chen, Z. Chen, A. Davis, J. Dean, M. Devin, S. Ghemawat, G. Irving, M. Isard, M. Kudlur, J. Levenberg, R. Monga, S. Moore, D. G. Murray, B. Steiner, P. Tucker, V. Vasudevan, P. Warden, M. Wicke, Y. Yu and X. Zheng, TensorFlow: A system for large-scale machine learning, 2016, arXiv:1605.08695.
- [2] N. Adebar, J. Keupp, V. N. Emenike, J. Kühnborn, L. vom Dahl, R. Möckel and J. Smiatek, Scientific Deep Machine Learning Concepts for the Prediction of Concentration Profiles and Chemical Reaction Kinetics: Consideration of Reaction Conditions, *The Journal of Physical Chemistry A*, **128** (2024), 929–944.
- [3] T. Akiba, S. Sano, T. Yanase, T. Ohta and M. Koyama, Optuna: A next-generation hyperparameter optimization framework, in *The 25th ACM SIGKDD International Conference on Knowledge Discovery & Data Mining*, 2019, 2623–2631.
- [4] R. H. Byrd, P. Lu, J. Nocedal and C. Zhu, A Limited Memory Algorithm for Bound Constrained Optimization, *SIAM Journal on Scientific Computing*, **16** (1995), 1190–1208.
- [5] S. Cai, Z. Mao, Z. Wang, M. Yin and G. E. Karniadakis, Physics-informed neural networks (PINNs) for fluid mechanics: A review, *Acta Mechanica Sinica*, **37** (2021), 1727–1738.
- [6] C. Cheng and G.-T. Zhang, Deep Learning Method Based on Physics Informed Neural Network with Resnet Block for Solving Fluid Flow Problems, *Water*, **13** (2021), 423.
- [7] S. Cuomo, V. S. Di Cola, F. Giampaolo, G. Rozza, M. Raissi and F. Piccialli, Scientific Machine Learning Through Physics-Informed Neural Networks: Where we are and What's Next, *Journal of Scientific Computing*, **92** (2022), 88.
- [8] Y. N. Dauphin, R. Pascanu, C. Gulcehre, K. Cho, S. Ganguli and Y. Bengio, Identifying and attacking the saddle point problem in high-dimensional non-convex optimization, in *Proceedings of the 27th International Conference on Neural Information Processing Systems - Volume 2*, NIPS'14, MIT Press, Cambridge, MA, USA, 2014, 2933–2941.
- [9] N. Dirkes, F. Key and M. Behr, Eulerian Formulation of the Tensor-Based Morphology Equations for Strain-Based Blood Damage Modeling, 2024, arXiv:2402.09319.
- [10] V. Dwivedi, N. Parashar and B. Srinivasan, Distributed physics informed neural network for data-efficient solution to partial differential equations, *Neurocomputing*, **420** (2021), 299–316.
- [11] H. Eivazi, M. Tahani, P. Schlatter and R. Vinuesa, Physics-informed neural networks for solving Reynolds-averaged Navier-Stokes equations, *Physics of Fluids*, **34** (2022), 075117.
- [12] S. A. Faroughi, N. M. Pawar, C. Fernandes, M. Raissi, S. Das, N. K. Kalantari and S. K. Mahjour, Physics-Guided, Physics-Informed, and Physics-Encoded Neural Networks and Operators in Scientific Computing: Fluid and Solid Mechanics, *Journal of Computing and Information Science in Engineering*, 1–45.
- [13] E. Haghghat, M. Raissi, A. Moure, H. Gomez and R. Juanes, A physics-informed deep learning framework for inversion and surrogate modeling in solid mechanics, *Computer Methods in Applied Mechanics and Engineering*, **379** (2021), 113741.
- [14] C. Haringa, *Through the Organisms Eyes*, PhD thesis, Delft University of Technology, 2017.
- [15] M. Islam, M. S. H. Thakur, S. Mojumder and M. N. Hasan, Extraction of material properties through multi-fidelity deep learning from molecular dynamics simulation, *Computational Materials Science*, **188** (2021), 110187, URL <https://www.sciencedirect.com/science/article/pii/S0927025620306789>.
- [16] A. D. Jagtap and G. E. Karniadakis, Extended Physics-Informed Neural Networks (XPINNs): A Generalized Space-Time Domain Decomposition Based Deep Learning Framework for Non-linear Partial Differential Equations, *Communications in Computational Physics*, **28** (2020), 2002–2041.

- [17] A. D. Jagtap, E. Kharazmi and G. E. Karniadakis, Conservative physics-informed neural networks on discrete domains for conservation laws: Applications to forward and inverse problems, *Computer Methods in Applied Mechanics and Engineering*, **365** (2020), 113028.
- [18] A. D. Jagtap, Z. Mao, N. Adams and G. E. Karniadakis, Physics-informed neural networks for inverse problems in supersonic flows, *Journal of Computational Physics*, **466** (2022), 111402.
- [19] X. Jin, S. Cai, H. Li and G. E. Karniadakis, NSFnets (Navier-Stokes Flow nets): Physics-informed neural networks for the incompressible Navier-Stokes equations, *Journal of Computational Physics*, **426** (2021), 109951.
- [20] E. Kharazmi, Z. Zhang and G. E. Karniadakis, Variational Physics-Informed Neural Networks For Solving Partial Differential Equations, 2019, arXiv:1912.00873.
- [21] G. Kissas, Y. Yang, E. Hwuang, W. R. Witschey, J. A. Detre and P. Perdikaris, Machine learning in cardiovascular flows modeling: Predicting arterial blood pressure from non-invasive 4d flow mri data using physics-informed neural networks, *Computer Methods in Applied Mechanics and Engineering*, **358** (2020), 112623, URL <https://www.sciencedirect.com/science/article/pii/S0045782519305055>.
- [22] P. L. Lagari, L. H. Tsoukalas, S. Safarkhani and I. E. Lagaris, Systematic Construction of Neural Forms for Solving Partial Differential Equations Inside Rectangular Domains, Subject to Initial, Boundary and Interface Conditions, *International Journal on Artificial Intelligence Tools*, **29** (2020), 2050009.
- [23] I. E. Lagaris, A. Likas and D. I. Fotiadis, Artificial neural networks for solving ordinary and partial differential equations, *IEEE Transactions on Neural Networks*, **9** (1998), 987–1000.
- [24] Z. Lai, C. Mylonas, S. Nagarajaiah and E. Chatzi, Structural identification with physics-informed neural ordinary differential equations, *Journal of Sound and Vibration*, **508** (2021), 116196.
- [25] S. Li and X. Feng, Dynamic Weight Strategy of Physics-Informed Neural Networks for the 2D Navier–Stokes Equations, *Entropy*, **24** (2022), 1254.
- [26] L. Lu, X. Meng, Z. Mao and G. E. Karniadakis, DeepXDE: A Deep Learning Library for Solving Differential Equations, *SIAM Review*, **63** (2021), 208–228.
- [27] R. Mojgani, M. Balajewicz and P. Hassanzadeh, Kolmogorov n–width and Lagrangian physics-informed neural networks: A causality-conforming manifold for convection-dominated PDEs, *Computer Methods in Applied Mechanics and Engineering*, **404** (2023), 115810.
- [28] B. Moseley, A. Markham and T. Nissen-Meyer, Solving the wave equation with physics-informed deep learning, 2020, arXiv:2006.11894.
- [29] B. Moseley, A. Markham and T. Nissen-Meyer, Finite basis physics-informed neural networks (FBPINNs): A scalable domain decomposition approach for solving differential equations, *Advances in Computational Mathematics*, **49** (2023), 62.
- [30] D. C. Psychogios and L. H. Ungar, A hybrid neural network-first principles approach to process modeling, *AIChE Journal*, **38** (1992), 1499–1511.
- [31] M. Raissi, P. Perdikaris and G. Karniadakis, Physics-informed neural networks: A deep learning framework for solving forward and inverse problems involving nonlinear partial differential equations, *Journal of Computational Physics*, **378** (2019), 686–707.
- [32] M. Raissi, A. Yazdani and G. E. Karniadakis, Hidden fluid mechanics: Learning velocity and pressure fields from flow visualizations, *Science*, **367** (2020), 1026–1030, URL <https://www.science.org/doi/abs/10.1126/science.aaw4741>.
- [33] A. Rosseburg, J. Fitschen, J. Wutz, T. Wucherpennig and M. Schlüter, Hydrodynamic inhomogeneities in large scale stirred tanks – Influence on mixing time, *Chemical Engineering Science*, **188** (2018), 208–220.
- [34] T. Sahin, M. von Danwitz and A. Popp, Solving Forward and Inverse Problems of Contact Mechanics using Physics-Informed Neural Networks, 2023, arXiv:2308.12716.
- [35] F. Sahlí Costabal, Y. Yang, P. Perdikaris, D. E. Hurtado and E. Kuhl, Physics-Informed Neural Networks for Cardiac Activation Mapping, *Frontiers in Physics*, **8**.
- [36] H. Sheng and C. Yang, PFNN: A penalty-free neural network method for solving a class of second-order boundary-value problems on complex geometries, *Journal of Computational Physics*, **428** (2021), 110085.
- [37] K. Shukla, A. D. Jagtap and G. E. Karniadakis, Parallel physics-informed neural networks via domain decomposition, *Journal of Computational Physics*, **447** (2021), 110683.

- [38] L. Sun, H. Gao, S. Pan and J.-X. Wang, Surrogate modeling for fluid flows based on physics-constrained deep learning without simulation data, *Computer Methods in Applied Mechanics and Engineering*, **361** (2020), 112732, URL <https://www.sciencedirect.com/science/article/pii/S004578251930622X>.
- [39] T. E. Tezduyar, M. Behr and J. Liou, A new strategy for finite element computations involving moving boundaries and interfaces—The deforming-spatial-domain/space-time procedure: I. The concept and the preliminary numerical tests, *Computer Methods in Applied Mechanics and Engineering*, **94** (1992), 339–351.
- [40] S. Tillmann, D. Hilger, N. Hosters and S. Elgeti, Shape-optimization of extrusion-dies via parameterized physics-informed neural networks, *PAMM*, **23** (2023), e202300203.
- [41] R. Van Der Meer, C. W. Oosterlee and A. Borovykh, Optimally weighted loss functions for solving PDEs with Neural Networks, *Journal of Computational and Applied Mathematics*, **405** (2022), 113887.
- [42] P. Virtanen, R. Gommers, T. E. Oliphant, M. Haberland, T. Reddy, D. Cournapeau, E. Burovski, P. Peterson, W. Weckesser, J. Bright, S. J. van der Walt, M. Brett, J. Wilson, K. J. Millman, N. Mayorov, A. R. J. Nelson, E. Jones, R. Kern, E. Larson, C. J. Carey, Í. Polat, Y. Feng, E. W. Moore, J. VanderPlas, D. Laxalde, J. Perktold, R. Cimrman, I. Henriksen, E. A. Quintero, C. R. Harris, A. M. Archibald, A. H. Ribeiro, F. Pedregosa and P. van Mulbregt, SciPy 1.0: Fundamental algorithms for scientific computing in Python, *Nature Methods*, **17** (2020), 261–272.
- [43] S. Wang, S. Sankaran, H. Wang and P. Perdikaris, An Expert’s Guide to Training Physics-informed Neural Networks, 2023, arXiv:2308.08468.
- [44] S. Wang, Y. Teng and P. Perdikaris, Understanding and Mitigating Gradient Flow Pathologies in Physics-Informed Neural Networks, *SIAM Journal on Scientific Computing*, **43** (2021), A3055–A3081.
- [45] S. Wang, X. Yu and P. Perdikaris, When and why PINNs fail to train: A neural tangent kernel perspective, *Journal of Computational Physics*, **449** (2022), 110768.
- [46] J. Yu, C. Yan and M. Guo, Non-intrusive reduced-order modeling for fluid problems: A brief review, *Proceedings of the Institution of Mechanical Engineers. Part G: Journal of Aerospace Engineering*, **233** (2019), 5896–5912.
- [47] W. Zhou, S. Miwa and K. Okamoto, Advancing fluid dynamics simulations: A comprehensive approach to optimizing physics-informed neural networks, *Physics of Fluids*, **36** (2024), 013615.
- [48] C. Zhu, R. H. Byrd, P. Lu and J. Nocedal, Algorithm 778: L-BFGS-B: Fortran subroutines for large-scale bound-constrained optimization, *ACM Transactions on Mathematical Software*, **23** (1997), 550–560.

Received xxxx 20xx; revised xxxx 20xx; early access xxxx 20xx.